University of Alberta

SUPERFLUIDITY NEAR LOCALIZATION: SUPERSOLID AND SUPERGLASS

by

Long Dinh Dang

A thesis submitted to the Faculty of Graduate Studies and Research in partial fulfillment of the requirements for the degree of **Doctor of Philosophy**.

in

Department of Physics

Fall 2010

Edmonton, Alberta

EXAMINING COMMITEE

Massimo Boninsegni (Supervisor), Physics

Kevin Beach, Physics

Mauricio Sacchi, Physics

Craig Heinke, Physics

Alex Brown, Chemistry

Mona Berciu, Physics, University of British Columbia

ABSTRACT

The main theme of this thesis is the interplay between superfluidity and localization, in a system of strongly correlated Bose particles. Driving this investigation is the search for yet unobserved phases of matter, such as the so-called *supersolid*. Using state-of-the-art, numerically exact computer simulations, we have carried out an extensive theoretical investigation of the effects of long-range interactions, inhomogeneity, disorder and frustration in a simple model of lattice Bosons. In particular, we explore the scenario of vacancy- and interstitial-based supersolid phases of hard core bosons on a square lattice, interacting repulsively via a nearest-neighbour and next-nearest neighbour potential. Secondly, in an attempt to model the physics of a layer of helium adsorbed on a corrugated substrate, an additional superlattice of the absorption sites is imposed to the system of hard core bosons, and the resulting low temperature phase diagram is studied. Finally, the possibility of actually *inducing by disorder* superfluidity (*superglass*) in a system that does not display it in the absence of disorder is demonstrated. The quantitative and qualitative predictions at which we have arrived appear to be at least in principle testable experimentally, for example by performing measurements on ultracold atoms in optical lattices.

ACKNOWLEDGEMENTS

I would like to express my gratitude to the University of Alberta for giving me the opportunity to work in a positive and stimulating scientific environment. First and foremost, I wish to thank my doctoral supervisor, Massimo Boninsegni, for providing, in addition to invaluable insight, the optimal conditions for a focus on scholarly research - though I am certain I at times did not take full advantage of them. Without his guidance and patient dedication, none of this work would have been possible. Also, I would like to acknowledge the collaborations with Lode Pollet, for his help with the numerical technique that was instrumental to the completion of the work.

Important interaction with people within my research group must also be acknowledged. From day-to-day mutual assistance, to frank discussions about our research, I have gained tremendously from the collaborations with Joseph Turnbull, Fabio Mezzacapo, Javier Cuervo, Piyush Jain, and Fabio Cinti. Many interesting ideas have been released from those interactions. In the same vein, I would like to acknowledge beneficial collaborations with other scientists, including P.-N. Roy in the department of chemistry for sharing his important insights over the course of my doctorate, as well as Evgeny Burovski and Giuliano Orso, both in Paris, for their help and for giving me a chance to present my research. Thanks also to Jim MacKinnon for his technical support.

Moreover, I also would like to acknowledge my family members for their support and dedication (con cam on ca nha rat nhieu!!!); my roommate Daniel Foster and his family for inviting me to their house during the year and for encouraging me to work on my research; my friends in Vietnamese Student Union for their helps every time I need.

Words have never been enough to thank my wife Cam Tu anh the little Panda for their compassion, dedication and sacrifice (Bo yeu hai me con!).

My work was supported by the Natural Sciences and Engineering Research Council of Canada (NSERC) through the PGSA and PGSB scholarship program, as well as through research Grant No. 121210893. Computing support from Westgrid and from AICT, University of Alberta is gratefully acknowledged, as is funding from the Alberta Informatics Circle of Research Excellence (ICORE) and the Faculty of Graduate Studies and Research.

Table of Contents

List of Figures

Chapter 1

Introduction

In this chapter, we briefly introduce the research theme of this thesis, which is superfluidity in physical settings where particles have the tendency to *localize*. Localization may arise from crystallization of the many-body system, occurring either spontaneously as a result of the interactions among elementary constituents, or induced by an external "pinning" potential or by confinement or disorder. We address several specific issues in this broad context by studying a simple model of lattice bosons, which allows one to answer a host of questions in a sufficiently general, unified language. The goal is not that of obtaining quantitative predictions for specific experimental systems (e.g., liquid helium), but rather that of gaining insight into the behaviour of superfluids near crystallization or in disorder.

1.1 The superfluid phenomenon

The year 1937 marked the discovery of the phenomenon of *superfluidity* (SF) which was first observed experimentally in bulk liquid ^{4}He independently by Kapitza [1] and by Allen and Misener [2]. It was found that ^{4}He undergoes a transition at the temperature $T_\lambda \approx 2.17K$ from a viscous fluid (referred to as a normal fluid) above T_λ to a fluid with practically no viscosity (referred to as a superfluid), capable of sustaining dissipationless flow below T_λ.

Superfluidity is perhaps the most spectacular manifestation of quantum mechanics on

a microscopic scale; as such, it is regarded as a low temperature phenomenon, i.e., it arises in a setting where the physical behaviour of the system is essentially dominated by its ground state properties. SF is related to Bose-Einstein condensation (BEC) phenomenon [3, 4], but the relationship is subtle, and in some regards still unclear [5]. For a translationally invariant system, BEC is equivalent to the occurrence of off-diagonal long range order (ODLRO). Bose statistics seems intimately connected to SF; indeed, the appearance of pairs of particles seems a necessary step in the stabilization of the superfluid phase of fermi systems, as pairs acquire integer spin, and can therefore be regarded as behaving like bosons, under specific circumstances.

In the form of persistent flow, SF has so far been experimentally observed only in the two isotopes of helium (^{4}He and ^{3}He), even though progress in the stabilization of assemblies of ultracold atoms may soon pave the way for the experimental study of SF in different, perhaps more controllable settings. The main obstacle to observing SF in other condensed matter systems that could potentially display it, such as molecular hydrogen, is the fact that at sufficiently low temperature crystallization occurs. As atoms or molecules become localized, transport is impeded and SF ceases to occur. Helium, on the other hand, under the pressure of its own vapour, remains a liquid all the way down to zero temperature (see, for instance, Ref. [6]).

In general, it seems natural to regard localization as an "enemy" of both BEC and SF, but an active line of theoretical and experimental investigation in low temperature physics aims at identifying specific physical systems and/or settings, in which SF and localization may coexist in a single, homogeneous phase of matter. The earliest proposal for this to occur was that of Andreev and Lifshitz, who, over four decades ago, speculated that a phase of matter known as *supersolid*, simultaneously displaying crystalline order (rigid, or diagonal long range order with broken translation symmetry) and superfluidity (superflow, and the concomitant off-diagonal long range order with broken *U(1)* gauge symmetry). Andreev and Lifshitz, as well as other authors [7, 8, 9], proposed that solid helium could be a candidate for the observation of such a supersolid phase, which has been sought experimentally for over fifty years. In 2004, E. Kim and M. W. Chan claimed to have finally succeeded in observing supersolid helium [10], but it seems fair to state that their claim is not universally accepted (due to the active debate about this possible phase)

at the time of this writing.

Other scenarios of SF in the presence of localization, such as in disordered systems, or in confined geometries, have been the subject of much experimental and theoretical investigation over the past two decades. Besides its unquestionable fundamental importance, the subject of SF in disorder or confinement is of interest due to the connection of SF to superconductivity [6], whose potential technological impact can hardly be overstated. Superconductivity occurs in crystals, i.e., systems which are inevitably "dirty," disordered by defects, impurities and so on.

This thesis is a contribution to the theoretical understanding of SF in condensed matter systems where particles are subjected to localization. We focus our attention on three specific scenarios, namely crystallization, occurring as a result of interactions among particles, induced by an external potential, and disorder. As an archetypal model of a superfluid, we adopted the lattice hardcore Bose model, with the addition of nearest-neighbour and next-nearest-neighbour interactions.

The choice of this model is motivated essentially by its simplicity. It is conceptually related to the Bose Hubbard model (BHM) [11], which is a minimal model of SF extensively used to gain insight into fundamental properties of the superfluid phase. The purpose of utilizing such a model in a theoretical study is generally not that of obtaining precise, quantitatively reliable theoretical predictions applicable to an actual experimental system, but rather that of determining broad conditions under which SF can manifest itself, possibly in concomitance with other types of order.

Over the past decade, however, this state of affairs has changed somewhat, as simple models such as the BHM can actually be regarded as realistic descriptions of assemblies of cold atoms trapped in optical lattices [12, 13, 14]. Thus, models regarded until over a decade ago as being of "academic interest" only, are now eliciting renewed attention, as potentially allowing for quantitative predictions for experimental systems realizable in the laboratory.

Our studies consist of state-of-the-art numerical simulations based on the Worm Algorithm (WA) [15, 16]. This computational tool belongs to the class of Quantum Monte Carlo (QMC) techniques, which are widely regarded as the method of choice to inves-

tigate equilibrium thermodynamic properties of Bose systems at finite temperature. The advantage of this methodology is that it allows one to obtain reliable numerical results, virtually exact and free from approximations, for a wide class of Bose systems, featuring very different interactions; it also provides direct access to relevant physical quantities that are used to characterize experimentally the superfluid phase of matter.

1.2 Summary of original research

In the course of this investigation, we carried out three separate, but conceptually related projects, namely:

1.2.1 Vacancy-based supersolidity

In this part of our research, we investigated the scenario of vacancy-based *supersolidity* near crystallization induced by interparticle interactions. This is the original proposal for a supersolid phase [7, 8], namely one displaying simultaneously crystalline order and superfluidity. In their scenarios, Andreev and Lifshitz hypothesized that point defects such as *vacancies* (where the particles are removed from the lattice sites) could enjoy high mobility, hop from one lattice site to an adjacent one, and essentially act as a weakly interacting dilute lattice Bose gas, which could undergo Bose condensation and enjoy frictionless flow. However, recent first-principles numerical simulations have yielded strong evidence that such a scenario does not actually occur in solid helium, as any dilute gas of weakly interacting vacancies would be unstable against separation of the system into two phases, one vacancy-free and the other rich in vacancies, which can then be removed from the system via an adjustment of the lattice constant [17].

Computational studies of lattice models such as the hardcore Bose one, have yielded evidence of supersolid phases for various lattice geometries [18, 19, 20, 21, 22, 23, 24, 25, 26]. In all such studies, however, the supersolid phase is based on *interstitials* (where the particles are inserted between lattice sites) rather than vacancies, i.e., there appears to be an asymmetry in the behaviour of such point defects. In contrast, doping with vacancies results in the coexistence of an insulating crystal and a superfluid by the formation of a

domain wall (e.g., a line of hole separated particles into two parts) [21]. Our study was aimed at elucidating the asymmetry between the behaviour of vacancies and interstitials.

We carried out calculations in the context of the hardcore Boson model on the square lattice, supplemented by nearest-neighbour and next-nearest-neighbour repulsive interactions. Our main results show that a vacancy-based supersolid phase is possible, and we obtained a simple criterion to predict its occurrence. We also studied the possible occurrence of a *commensurate* supersolid phase, namely one with neither vacancies nor interstitials, and found that no such phase exists, in accord with most other studies.

This research was published in

L. Dang, M. Boninsegni and L. Pollet. Phys. Rev. B **78**, 132512 (2008).

1.2.2 Supersolidity in a periodic superlattice

In this project, we considered another scenario of supersolidity near crystallization, this time not arising spontaneously but rather induced by an external potential. This study is qualitatively relevant to helium films adsorbed on graphite.

In this work, we investigated theoretically the possible existence of supersolid behaviour near a crystalline phase stabilized by an external periodic potential, which plays the same role as the adsorption sites of a corrugated substrate. Such a crystalline phase is *not* present in the phase diagram of the system in the absence of an external potential.

The purpose of this study is to provide a simple theoretical framework to interpret experimental studies probing for possible (commensurate) unconventional superfluid phases (or supersolid phases) of helium films on graphite. Our main finding is that these phases exist on both the interstitial and on the vacancy side of a commensurate (registered) crystal. A second, important conclusion of this study, is that the superfluid density *always vanishes* as the particle density hits a value corresponding to either a commensurate or incommensurate crystal. In this sense, the pinning potential does not give rise to fundamentally new behaviour, with respect to what is observed in this model near and/or at incommensurate crystal phases, in the absence of any external potential. The vanishing of the superfluid response at crystal density appears therefore to be a general hallmark of any phase labelled as "supersolid", occurring in a system of this type, i.e., in the presence

of an external pinning potential.

This research was published in:
L. Dang and M. Boninsegni, ArXiv:1003.1367 (2010)

1.2.3 Disorder-induced superfluidity

In this study, we investigated a different scenario of unconventional superfluidity, arising from the presence of disorder.

We consider a model of lattice hardcore bosons with a strong *attractive* nearest-neighbour interaction. Such a system does *not* display a superfluid phase in the absence of disorder.

We present here strong numerical evidence for disorder-induced superfluidity. Specifically, we show that at low temperature and in a small range of attractive interactions, disorder of sufficient strength stabilizes a "glassy" superfluid phase or *superglass*. Aside from supersolid ^{4}He, such a scenario is possibly relevant to other condensed matter systems, e.g., high-temperature superconductors [27], as well as to the elusive superfluid phase of bulk molecular hydrogen [28], and to the role of substrate disorder in the superfluidity of (sub)monolayer helium films [29, 30].

This research was published in:
L. Dang, M. Boninsegni and L. Pollet. Phys. Rev. B **79**, 214529 (2009),
and reprinted in Virtual Journal of Atomic Quantum Fluids **1**, 1 (2009).

1.3 Thesis outline

This thesis is organized as follows: in Chapter 2, we introduce the model of interacting bosons that is common to all the projects carried out in this work. Next, we describe the computational methodology in Chapter 3. In Chapter 4, we will discuss the results of our research efforts, and Chapter 5 summarizes the thesis.

Chapter 2

Lattice model for interacting bosons

In this chapter we introduce the model that constitutes the theoretical starting point for our studies. The hardcore Boson model can be seen as a particular case of the Bose Hubbard model, and we therefore start out by describing the latter. The Bose Hubbard model is a reasonable minimal model of such systems as granular superconductors, short correlation length superconductors, Josephson arrays, flux lattices in type II superconductors, helium films, and ultracold neutral bosonic atoms trapped in an optical lattice. In these realizations, bosons are either elementary particles, elementary excitations, or tightly bound composites of fermions that behave like effective Bose particles.

2.1 Bose Hubbard model

The Bose Hubbard Hamiltonian (BHM) [11] is expressed in second quantized language as follows:

$$H = -J \sum_{\langle ij \rangle} (\hat{b}_i^\dagger \hat{b}_j + h.c.) + \frac{1}{2} U \sum_i \hat{n}_i (\hat{n}_i - 1) - \mu \sum_i \hat{n}_i \tag{2.1}$$

here, a d-dimensional lattice of a given geometry with N sites is assumed, in which each site has a number z of nearest neighbouring sites. Henceforth, we shall be considering exclusively the case d = 2; on a square lattice, z = 4, whereas z = 6 on a triangular lattice. The operators $\hat{b}_i$ and $\hat{b}_i^\dagger$ annihilate and create a boson at the ith site, and obey the canonical

commutation relations

$$[\hat{b}_i, \hat{b}_j^\dagger] = \delta_{ij}$$

The number operator $\hat{n}_i = \hat{b}_i^\dagger \hat{b}_i$ counts the number of particles at lattice site i. The first term in (2.1) describes the hopping process of a particle between two nearest neighbouring sites, J being the hopping matrix element (also known as *hopping integral*); the sum $\langle ij \rangle$ runs over all $zN/2$ pairs of nearest-neighbouring sites. The second term describes the interaction between particles occupying the same lattice site. In general, U is positive, as particles occupying the same sites experience a repulsive interaction, typically arising from the repulsion of electrons belonging to the "clouds" of different atoms (such a repulsion originates from the Pauli exclusion principle, which prevents electrons from occupying the same quantum state). The last term in (2.1) represents the energy associated with having a given number of particles in the system, μ being the value of the chemical potential; in other words, we allow the number of particles to fluctuate in our studies, i.e., we work within the *Grand Canonical* ensemble. The particle density (or, filling) is $\rho = N_b/N$, where $N_b = \sum_i \hat{n}_i$ is the total number of particles in the system.

2.2 Physics of the Bose Hubbard model

The Bose Hubbard model was utilized by Fisher $et.\ al.$ [11] to describe the cessation of superfluidity due to strong interactions and disorder. It is possibly one of the simplest models of superfluidity (SF), exhibiting a quantum (i.e., ground state) phase transition known as the SF$-$Mott Insulator (MI) transition [11]. The Hubbard Hamiltonian can be used to describe the onset of superfluidity of helium on substrates such as graphite [31], the superconductor-insulator transition in materials with preformed Cooper pairs [32, 33], helium in disordered and restricted geometries [34, 35], spin-flip transitions in quantum spin systems in external magnetic fields [36] and so forth. Thanks to advances in technology, Greiner $et.\ al.$ [37] has recently implemented a suggestion by Jaksch $et.\ al.$ [12] to realize this model experimentally by trapping ultracold atoms in an optical lattice. This allowed for the experimental observation of the SF-MI transition. Indeed, it is now customary to refer colloquially to optical lattices as the "Hubbard toolbox" [13].

The BHM, in spite of its apparent simplicity, does not lend itself to an exact analytical

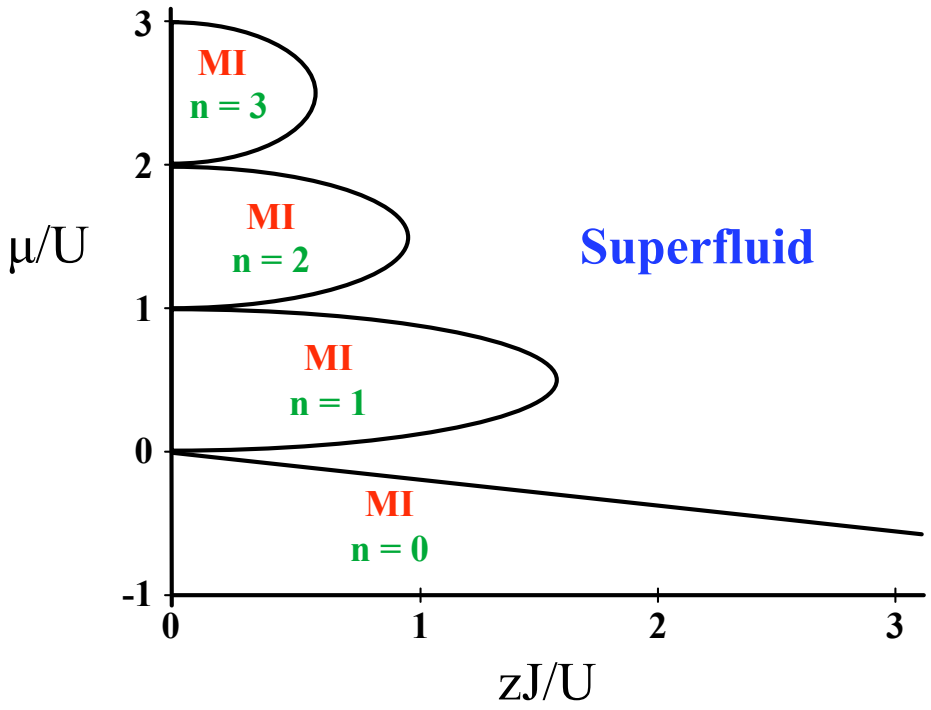

Figure 2.1: Mean field phase diagram of the ground state of the Bose Hubbard model (2.1). The vertical axis represents the chemical potential, μ; the horizontal axis represents the kinetic energy, which is characterized by the hopping amplitude J. Both μ and J are scaled with respect to the on site interaction, U. The notation MI refers to a Mott insulator with a number of particles per site equal to n. In this figure, z is the coordination number, i.e., the number of nearest-neighbouring sites.

treatment, except in the trivial $J = 0$ or $U = 0$ limits. However, the ground state phase diagram can be explored by mean-field type calculations [11, 38, 39, 40], as well as by numerical simulations. Such is illustrated in Fig. 2.1.

In the regions under the "lobes" of Fig. 2.1 (at small values J/U), the system displays insulating behaviour, as each lattice site is occupied on average by the same integer number of particles, and a large energy penalty U is paid if a particle hops to a nearest-neighbouring site. This type of insulator, where the particle density is uniform throughout the lattice, and particle localization arises from interactions rather than band structure, is known as *Mott Insulator*. On the other hand, in the rest of the phase diagram, the energy

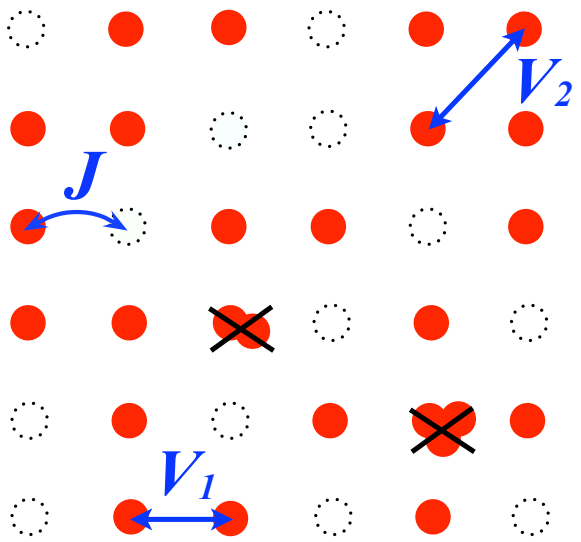

Figure 2.2: Schematic illustration of the hardcore limit of the HCBM with long-range interactions. Filled circles refer to particles, whereas the dashed circles refer to empty sites. V_1 refers to the nearest-neighbour interaction potential, V_2 to the next-nearest-neighbour interaction, and J to the hopping amplitude. Multiple occupation of sites is forbidden in the hardcore limit.

balance is dominated by the kinetic energy, particles are delocalized, and the system is superfluid.

In this work, we have for simplicity focused on the so-called *hardcore* limit of the BHM, namely we set the on site interaction $U = \infty$, thereby preventing occupation of any lattice site by more than one particle (Fig. 2.2). Therefore, the particle density ρ falls in the range $0 \leq \rho \leq 1$. Such a restriction is justified by the large relative value of the onsite interaction in many physical systems of interest (e.g., helium films adsorbed on graphite) and causes no loss of generality for the results obtained here. Henceforth, we shall implicitly assume the hardcore restriction, and following the convention adopted in the literature, we refer to the ensuing version of model (2.1) as the *Hardcore Boson Model* (HCBM).

The HCBM is a minimal model of superfluidity, but does not feature in its phase diagram crystalline phases (i.e., insulating phases with a density modulation whose pattern is not that of the underlying lattice). As we are interested in possible SF near such a

crystalline phase, we need to incorporate some additional terms into the HCBM, such as interactions among particles on different sites.

It is known that a sufficiently strong *repulsive* interaction between particles residing on nearest-neighbouring sites, causes the appearance of a ("checkerboard") crystal at half-filling, i.e., at density ρ = 1/2 on the square lattice [18], ρ = 1/3 (and 2/3) on the triangular lattice [22]. The presence of both nearest and next-nearest neighbour repulsive interactions promotes a "star" crystal at density ρ = 1/4 on the square lattice [20, 41], a "striped" crystal at ρ = 1/2 on the square lattice [18], as well as a striped crystal at ρ = 2/3 on the triangular lattice [42]. In the vicinity of these crystalline phases, stable interstitial-based supersolid phases have been observed by numerical simulations, but not vacancy-based supersolids [18, 19, 21, 22, 23, 24, 25, 26]. One of the goals of this investigation is precisely to understand the reason for such an asymmetry between vacancies and interstitials.

In the work illustrated here, it is assumed that interactions can exist between particles residing on nearest-neighbouring and next-nearest-neighbouring sites. Thus, the general form of the model utilized here is the following:

$$H = -J \sum_{\langle ij \rangle} (\hat{b}_i^\dagger \hat{b}_j + h.c.) + V_1 \sum_{\langle ij \rangle} \hat{n}_i \hat{n}_j + V_2 \sum_{\langle\langle ij \rangle\rangle} \hat{n}_i \hat{n}_j - \sum_i \mu_i \hat{n}_i \qquad (2.2)$$

with an implicit restriction to no more than one particle per site. Here, the sum $\langle\langle ij \rangle\rangle$ runs over all pairs of next-neighbouring sites. For simplicity we shall refer to the above Hamiltonian as the "V_1" model if V_2 = 0 (i.e., only nearest-neighbour interaction is included), as well as "$V_1 - V_2$" model if we both V_1 and V_2 are nonzero. Fig. 2.2 schematically summarizes this model. Throughout this thesis, we set the hopping amplitude to be a unit of energy scale (J = 1).

The inclusion of a site-dependent chemical potential in the last term of (2.2) allows for an external potential, which will be utilized in two of the projects described in the remainder of this thesis.

The computational work described in the following chapter consists of an exploration of the phase diagram of (2.2) in two dimensions (2D), for different choices of lattice geometries, parameters V_1 and V_2 and external potential. We work in 2D not only because such a setting mimics the experimental situation encountered in some of the systems

of interest (e.g., helium films), but also because in 2D effect of interactions, quantum-mechanics and confinement can give rise to interesting, non-trivial phases.

Chapter 3

Methodology and simulation

In this chapter, we first discuss the quantum Monte Carlo (QMC) method in quantum statistical mechanics and then introduce a simple Monte Carlo sampling scheme called the Metropolis algorithm. Next, we discuss the worm algorithm, a particular implementation of QMC employed for lattice boson systems. After that, we highlight the topic of convergence in Monte Carlo calculations, with a discussion of statistical errors and equilibrium estimation.

3.1 Path integral Monte Carlo

3.1.1 Quantum statistics

In quantum statistics, for a many-body system with N *indistinguishable* particles in thermal equilibrium at temperature *T*, one wishes to evaluate the thermal average of an observable A, say, e.g. an internal energy. This quantity can be written as

$$\begin{aligned} \langle A \rangle &= \frac{1}{Z} \mathrm{Tr} \left\{ A e^{-\frac{H}{k_B T}} \right\} \\ &= \frac{1}{Z} \mathrm{Tr} \left\{ A e^{-\beta H} \right\} \end{aligned} \tag{3.1}$$

where $\langle \ldots \rangle$ stands for the thermal average; $\beta = 1/k_B T$ is the inverse temperature and k_B is the Boltzmann constant (for simplicity, we can set $k_B = 1$) ; H is the Hamiltonian of a

given system; and Z is the partition function, which has the following form:

$$Z = \text{Tr}\left\{e^{-\beta H}\right\} \tag{3.2}$$

A direct analytical calculation of (3.2) for systems with a non-trivial Hamiltonian (e.g. the many-body density matrix of an interacting system) is generally not possible, as its calculation would require the knowledge of the full spectrum of the Hamiltonian. Fortunately, the Monte Carlo technique can be used to compute such expressions exactly. In the following, we will describe how such a Monte Carlo calculation would proceed.

The Hamiltonian of a quantum system is unlike that of a classical system in that we do not trivially know its exact eigenvalues. However, we can map a d-dimensional quantum system onto a $(d+1)$-dimensional classical system. As a consequence, a quantum Monte Carlo algorithm can be performed for this higher dimensional classical system. In order to perform this procedure, we essentially need to express the partition function Z within a path integral representation.

To illustrate the QMC method, we can start with a conventional scheme [43, 44] by discretizing imaginary time (inverse temperature) $\beta = M\Delta\tau$, where M is the number of "time slices" and $\Delta\tau$ is the time step. The exponential in the partition function (3.2) is then re-written formally as follows:

$$e^{-\beta H} = \left(e^{-\Delta\tau H}\right)^M = (1 - \Delta\tau H)^M + O(\Delta\tau) \tag{3.3}$$

In the limit $M \to \infty(\Delta\tau \to 0)$, the equation (3.3) becomes exact. Furthermore, the partition function Z is represented by a sum over all basis states of the identity matrix $\sum_i |i\rangle\langle i| = I$, so that

$$\begin{aligned} Z &= \text{Tr}[\exp(-\beta H)] = \text{Tr}[(1 - \Delta\tau H)^M] + O(\Delta\tau) \\ &= \sum_{i_1,\ldots,i_M} \langle i_1|1 - \Delta\tau H|i_2\rangle\langle i_2|1 - \Delta\tau H|i_3\rangle \ldots \langle i_M|1 - \Delta\tau H|i_1\rangle + O(\Delta\tau) \end{aligned} \tag{3.4}$$

The way in which we have written the partition function in (3.4) is called the *path integral representation*. Unfortunately, at this level, the immense multidimensional character of the problem ($d \times N \times M$, for a d-dimensional system of N particles with M discretization points of β) makes such an approach scale unfavorably. Indeed, the large number of

coupled degrees of freedom inherent to the problem renders viable only one approach for calculating the sum in (3.4), Monte Carlo integration. The sampling of the vast configuration space is then performed stochastically.

For simplicity, we can choose the basis states $|i\rangle$ as the eigenstates of the local operators such as a particle operator $\hat{n}_i$ in the HCBM (2.2) or a spin operator $\hat{S}_z$ in the spin-1/2 XXZ quantum Heisenberg model [45]. For the purpose of mapping the quantum Monte Carlo picture onto a standard classical one such as Monte Carlo for the Ising model [46], we specifically choose the basis states of the spin system. Each such state corresponds to one of the possible configurations of the classical spin systems with probabilities given by the matrix elements $\langle i_n|1 - \Delta\tau H|i_{n+1}\rangle$. At this stage, we can in principle perform a conventional Monte Carlo calculation for the Ising-like system in $(d + 1)$ dimensions where the extra dimension is the imaginary time axis (determined by β). The evolution of a particle in imaginary time defines its path (also referred to as a *world-line* of the particle)

We should note that the efficiency of Monte Carlo methods depends on the specific way in which the partition function Z (3.2) is sampled. As a result, different algorithms employ different approaches to sample this partition function (3.2).

3.1.2 Path sampling and the Metropolis algorithm

How does one go about generating a statistical ensemble of world-lines? The simplest sampling scheme is known as the Metropolis algorithm [47]. In the Metropolis algorithm, one samples the partition function Z (3.2) according to a statistical probability or a weight function $W(\mathbf{x})$ in a configuration $\mathbf{x}$ with which it is distributed. As a result, the thermal observable A (3.1) within this sampling scheme can be written in the following form:

$$\langle A\rangle = \frac{\sum_{t=0}^{\infty} A(\mathbf{x})W(\mathbf{x})}{\sum_{t=0}^{\infty} W(\mathbf{x})} \tag{3.5}$$

where t is a sequence of random variables defined in the configuration $\mathbf{x}$. In principle, one has to be able to go through all points $\mathbf{x}_i$ in configuration space with a finite number of steps in any simulation. In practice, however, it is impossible to create a distribution of points in configuration space which matches some arbitrary $W(\mathbf{x})$. Providentially, there

is, however, a strategy which produces statistically dependent samples based on the idea of a Markov process [48]. It starts from an initial point $\mathbf{x}_0$ and the subsequent states are generated through a sequential chain (known as Markov chain):

$$\mathbf{x}_0 \rightarrow \mathbf{x}_1 \rightarrow \ldots \rightarrow \mathbf{x}_n \rightarrow \mathbf{x}_{n+1} \rightarrow \ldots \tag{3.6}$$

The transition probability of going from a state $\mathbf{x}_i$ to a state $\mathbf{x}_j$ in one step of the Markov chain is denoted by a transition matrix $T(\mathbf{x}_i \rightarrow \mathbf{x}_j)$. The columns of the matrix T are normalized such that the sum of the probabilities of going from state $\mathbf{x}_i$ to any state is one:

$$\sum_{\mathbf{x}_j} T(\mathbf{x}_i \rightarrow \mathbf{x}_j) = 1 \tag{3.7}$$

The more efficient a Markov process is, the faster the simulations converge. Therefore, the improvement of Markov chain performance is at the heart of developments in Monte Carlo algorithms. The most important procedure is to determine the transition matrix T so that we asymptotically approach the desired probability $W(\mathbf{x})$. For an approach to work, two statistical conditions must be satisfied. The first condition is *ergodicity* which states that it has to be possible to reach any point $\mathbf{x}_i$ from any other point $\mathbf{x}_j$ in configuration space after a finite number of Markov steps. The second condition is *detailed balance* whereby the distribution function $W(\mathbf{x})^{(N)}$ at each step of the Markov process satisfies an equation:

$$\sum_{\mathbf{x}_i} W(\mathbf{x}_i)^{(N)} T(\mathbf{x}_i \rightarrow \mathbf{x}_j) = W(\mathbf{x}_j)^{(N+1)} \tag{3.8}$$

Although, the probability $W(\mathbf{x})^{(\mathbf{N})}$ changes at each step, it converges to the equilibrium distribution $W(\mathbf{x})$ after many steps. This function is an eigenfunction with eigenvalue 1, and the equilibrium condition reads:

$$\sum_{\mathbf{x}_i} W(\mathbf{x}_i) T(\mathbf{x}_i \rightarrow \mathbf{x}_j) = W(\mathbf{x}_j) \tag{3.9}$$

Then, for the detailed balanced condition to be satisfied, we must have

$$T(\mathbf{x}_i \rightarrow \mathbf{x}_j) W(\mathbf{x}_i) = T(\mathbf{x}_j \rightarrow \mathbf{x}_i) W(\mathbf{x}_j) \tag{3.10}$$

Markov chains that satisfy (3.10) are called reversible processes. The Metropolis algorithm satisfies both the ergodicity and detailed balance conditions.

The Metropolis algorithm works very well to simulate a system at high temperature, which is far away from the transition temperature T_C in a second order phase transition. Unfortunately, it does not work well in the temperature region close to T_C due to a well-known problem called "critical slowing down" [46]. One remarkable solution for this problem is to utilize cluster update, or the *loop* algorithm. There are two important variants of the loop algorithm: the first one is the Swendsen-Wang algorithm [49], which is based on multiple cluster updates, and the second one is the Wolff algorithm [50] which based on large single-cluster updates.

These loop algorithms perform very well for quantum spin systems, in the absence of an external magnetic field, but become far less effective when a magnetic field is switched on. Moreover, for magnetic models without spin inversion symmetry as well as particle models without particle-hole symmetry, the loop algorithm cannot be applied. Therefore, two alternative algorithms have been developed to solve these problems. One is the *directed-loop* algorithm by Sandvik *et. al.* [51, 52] and the other is the worm algorithm (WA) by N. Prokof'ev *et. al.* [15, 16]. The main idea of these algorithms is to break the world-line into a segment with two discontinuities and then explore the configuration space. We employ WA for the HCBM throughout this dissertation, and will discuss the worm algorithm in more detail in the next section.

3.2 Worm algorithm

In this section, we follow the approach by Prokof'ev [53]. We start with the formalism of path integrals for lattice systems. Next, we introduce an extended configuration space from which the worm algorithm is derived. Finally, we will discuss in more detail the most recent improvement to the worm algorithm, namely the worm algorithm locally optimal updates [54].

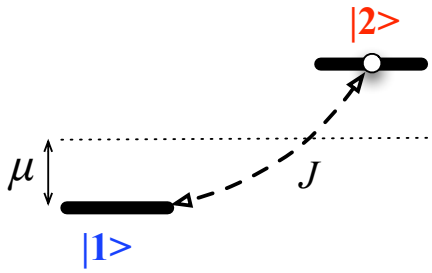

Figure 3.1: An illustration of the two level system which consists of site 1, corresponding to the state $|1\rangle$, and site 2, corresponding to the state $|2\rangle$; J is a transition amplitude and μ is an biased energy.

3.2.1 Two level system

We start with the simplest non-trivial system, namely the two level system shown in Fig. 3.1. For the sake of discussion, let us assume that we have only two sites, which are represented by two corresponding states $|1\rangle$ and $|2\rangle$. The Hamiltonian of the two level system in this representation reads:

$$H = J\hat{\sigma}_z - \mu\hat{\sigma}_x \tag{3.11}$$

where $\hat{\sigma}$ are the usual Pauli matrices:

$$\hat{\sigma}_x = \begin{pmatrix} 0 & 1 \\ 1 & 0 \end{pmatrix}, \hat{\sigma}_y = \begin{pmatrix} 0 & i \\ -i & 0 \end{pmatrix}, \hat{\sigma}_z = \begin{pmatrix} 1 & 0 \\ 0 & -1 \end{pmatrix}$$

We can consider J in the Hamiltonian (3.11) as a transition amplitude and μ as a biased energy. In principle, their role can be switched if we make a rotation of the Hamiltonian (3.11) by describing it in another basis set, for example $|a, b\rangle = \frac{1}{\sqrt{2}}(|1\rangle \pm |2\rangle)$. It is trivial to find the ground state energy $E_g = -E = -\sqrt{J^2 + \mu^2}$ as well as the excited state energy $E_e = E = \sqrt{J^2 + \mu^2}$ with corresponding eigenstates:

$$|g\rangle = \sin\theta|1\rangle + \cos\theta|2\rangle, |e\rangle = \cos\theta|1\rangle - \sin\theta|2\rangle$$

The partition function of the two level system reads:

$$Z = \sum_{\alpha=g,e\equiv 1,2} e^{-\beta H} \tag{3.12}$$

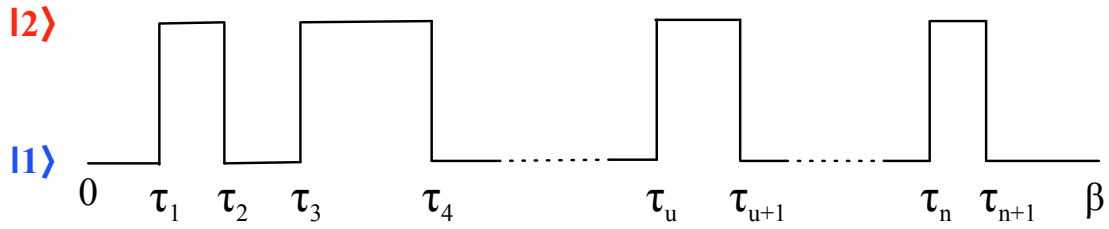

Figure 3.2: An example of a trajectory for a single particle which describes the evolution of this particle in configuration space in the two level system characterized by two states $|1\rangle$ and $|2\rangle$. A single particle hops from site 1 to site 2 and vice versa, creating the kinks illustrated by the vertical lines, whereas the horizontal lines illustrate the period of time this particle spends at site 1 (or 2). The positions of these kinks are marked by τ_i on the imaginary time axis.

where H is the Hamiltonian (3.11) and β is the inverse temperature. Now, we write the partition function Z (3.12) in the *path integral representation* of the two level system states $|1,2\rangle$:

$$Z = \sum_{\alpha_1,\ldots,\alpha_{L-1}=1,2} \langle\alpha_0|e^{-Hd\tau}|\alpha_{L-1}\rangle\langle\alpha_{L-1}|\ldots\langle\alpha_1|e^{-Hd\tau}|\alpha_L \equiv \alpha_0\rangle \tag{3.13}$$

where $\beta = Md\tau$, the number of terms in the product $M = \beta/d\tau \to \infty$, and the constraint $\alpha_L = \alpha_0$ is required since we are calculating the *trace*. The sum (3.13) is taken over all possible sequences $\alpha_0, \alpha_1, \ldots, \alpha_{L-1}, \alpha_L \equiv \alpha_0$ which form a path or a trajectory $\alpha(\tau)$ in $\alpha-$space. Fig. 3.2 shows an example of one possible trajectory in $\alpha-$space. It is necessary to calculate the matrix elements $\langle\alpha'|e^{-Hd\tau}|\alpha\rangle$ in the limit of $d\tau \to 0$, giving us the contribution of a given path to the transition amplitude. Since, in the limit of small $d\tau$, $e^{-Hd\tau} \approx 1 - Hd\tau$, we arrive at the final contribution to the probability:

$$\langle\alpha'|e^{-Hd\tau}|\alpha\rangle \approx \begin{cases} e^{-\mu_\alpha d\tau} & ,\mu_{\alpha=1,2} = \pm\mu \quad (\text{If } |\alpha'\rangle = |\alpha\rangle) \\ Jd\tau & (\text{If } |\alpha'\rangle \neq |\alpha\rangle) \end{cases} \tag{3.14}$$

As a result, we can write the partition function (3.13) in the integral form:

$$Z = \sum_{n=0}^{\infty} \int_0^\tau d\tau_1 \int_{\tau_1}^\tau d\tau_2 \ldots \int_{\tau_{n-1}}^\tau d\tau_n (iJ)^n e^{-i\mu_{\alpha_0}(\tau_1-0)-i\mu_{\alpha_1}(\tau_2-\tau_1)\ldots-i\mu_{\alpha_n}(\tau-\tau_n)} \tag{3.15}$$

where the sum as well as the integral are taken over all allowed trajectories. The formula (3.15) is the *path integral* of the partition function for the two level system.

3.2.2 Lattice path integral for a single particle system

Based on the path integral for the two level system, we are ready to generalize to the case in which a single particle not only hops over two sites but over many sites in the uniform $d-$dimensional lattice. The Hamiltonian reads:

$$H = -J \sum_{<ij>} (\hat{b}_i^\dagger \hat{b}_j + h.c.) + \sum_i \mu_i \hat{n}_i \tag{3.16}$$

Where J is the transition amplitude between the nearest neighbour sites and μ_i is the biased energy of the particle on site i; the operator $\hat{b}_i$ ($\hat{b}_i^\dagger$) is the annihilation (creation) operator which annihilates (creates) a particle at site i. The Hamiltonian (3.16) is written in the site representation; therefore $\hat{n}_i$ plays the role of the particle operator acting on site i which gives rise to the particle number. It is standard to separate the Hamiltonian (3.16) into two parts in the representation $|\alpha\rangle = \{|n_i\rangle\}$: one is a diagonal term called U and the other is an off-diagonal term called K:

$$H = K + U; \;\; K = -J \sum_{<ij>} (\hat{b}_i^\dagger \hat{b}_j + h.c.) \quad \text{and} \quad U = \sum_i \mu_i \hat{n}_i \tag{3.17}$$

where:

$$K|\alpha\rangle = \sum_{\varphi \neq \alpha} K_{\varphi\alpha} |\varphi\rangle; K_{\alpha\alpha} = 0 \tag{3.18}$$

$$U|\alpha\rangle = U_\alpha |\alpha\rangle; \tag{3.19}$$

The partition function Z for a single particle system can be written similarly to that of the two level system (3.13):

$$Z = \sum_{\{\alpha_i\}, \alpha_L = \alpha_0} \langle \alpha_L | e^{-d\tau H} | \alpha_{L-1} \rangle \ldots \langle \alpha_1 | e^{-d\tau H} | \alpha_0 \rangle \tag{3.20}$$

In the limit of $d\tau \to 0$, we use the approximation:

$$e^{-d\tau H} = 1 - d\tau K - d\tau U + O(\Delta\tau^2) \tag{3.21}$$

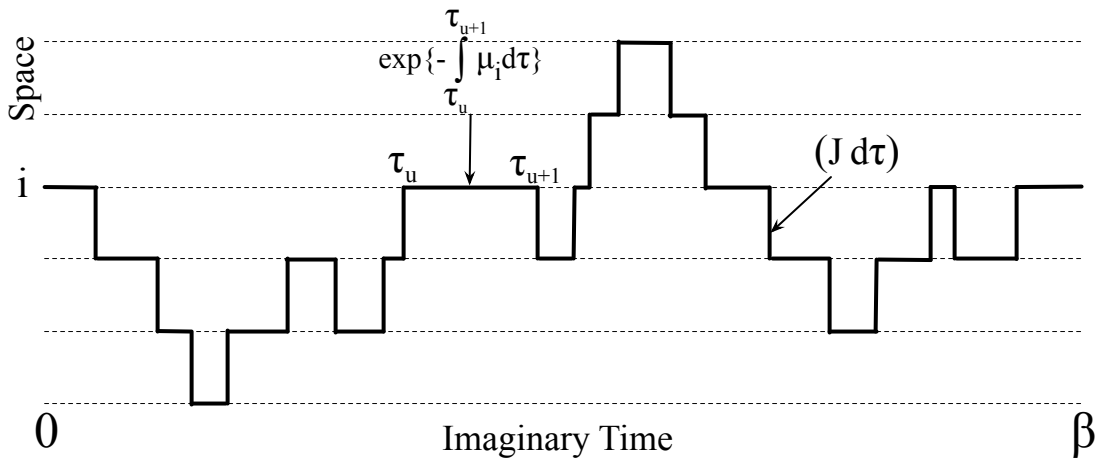

Figure 3.3: (Solid line) A trajectory for a single particle which describes the evolution of the particle in the configuration space of a one-dimensional lattice with 6 sites. A single particle hops from one site to its nearest neighbour sites, creating the kinks illustrated by the vertical lines, whereas the horizontal lines illustrate the period of time this particle spends at a lattice site. (Dashed lines) The regions in configuration space which are not occupied by the particle during its evolution.

Hence, it is straightforward to evaluate a configuration weight for the diagonal part:

$$W_d = \langle\alpha|e^{-d\tau H}|\alpha\rangle \approx e^{-d\tau U_\alpha} \tag{3.22}$$

as well as the configuration weight for the off-diagonal part:

$$W_o = \langle\alpha|e^{-d\tau H}|\varphi \neq \alpha\rangle \approx -d\tau K_{\alpha\varphi} \tag{3.23}$$

As a result, the configuration weight of the system is:

$$W_\nu = \exp\left\{-\int_0^\beta d\tau U_{\alpha(\tau)}\right\} \prod_{i=1}^{L} \left(-d\tau K_{\alpha_i\alpha_{i+1}}\right) \tag{3.24}$$

where L is the number of the configuration weights of the off-diagonal part in which the transition changes from the state α_i to $\alpha_{i+1} \neq \alpha_i$. The evolution of the single particle in a space-time configuration is illustrated in Fig. 3.3. The partition function (3.20) can be expressed in terms of the configuration weights W_ν:

$$\begin{aligned} Z &= \sum_{L=0}^{\infty} \int_0^\beta d\tau_1 \ldots \int_{\tau_{L-1}}^\beta d\tau_L \sum_\nu W_\nu \qquad (3.25) \\ &= \sum_{L=0}^{\infty} \int_0^\beta d\tau_1 \ldots \int_{\tau_{L-1}}^\beta d\tau_L \sum_{\alpha_0,\ldots,\alpha_L=\alpha_0} \exp\left\{-\sum_{i=1}^{L} \int_{\tau_{i-1}}^{\tau_i} d\tau U_{\alpha(\tau_i)}\right\} \prod_{i=1}^{L} \left(-K_{\alpha_i\alpha_{i+1}}\right) \end{aligned}$$

where the sum is taken over all possible trajectories in the configuration space, and $\tau_0 = \tau_L$, by definition, in imaginary time. For the Hamiltonian (3.16), the partition function is further simplified as:

$$Z = \sum_{L=0}^{\infty} (J)^L \int_0^\beta d\tau_1 \ldots \int_{\tau_{L-1}}^\beta d\tau_L \sum_{i_{CP}(\tau)} \exp\left\{-\sum_{i=1}^{L} \int_{\tau_{i-1}}^{\tau_i} \mu_{i(\tau)} d\tau\right\} \tag{3.26}$$

where the sum is over all the closed path $i_{CP}(\tau)$. Although the partition function (3.26) is written for a single particle, it is generally applicable for any lattice system which is separable into two parts, such as (3.17).

3.2.3 Lattice path integral for the many body system

The many body system includes additional terms in the Hamiltonian (3.16), namely the interaction terms with a general form $\sum_{i,j} V(i,j) n_i n_j$. If the hardcore constraint, nearest-neighbour and next-nearest-neighbour interactions are taken into account, we recover the

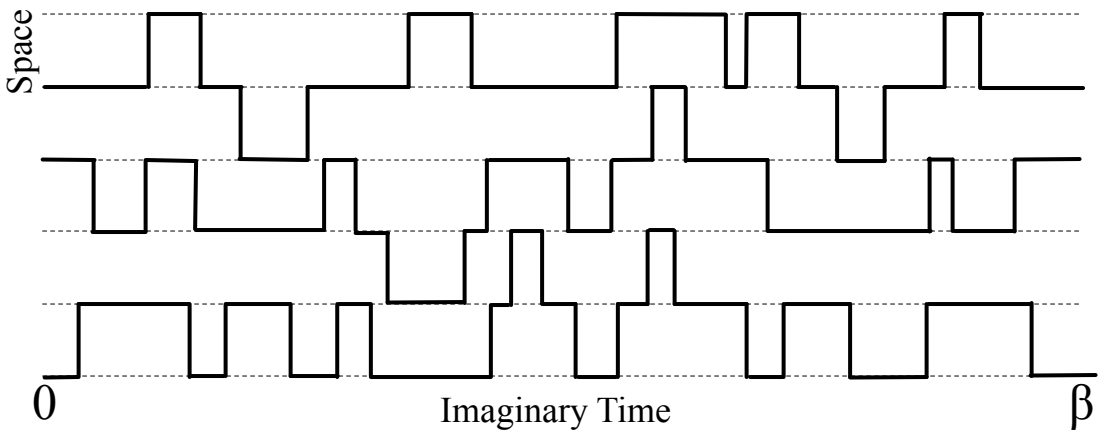

Figure 3.4: (Solid lines) Trajectories of three hardcore bosons which describe the evolution of their world-lines in a one-dimensional configuration space with 6 lattice sites. The bosons hop from one site to their nearest-neighbour sites, creating kinks illustrated by the vertical lines, whereas the horizontal lines illustrate the period of time particles spend at the same lattice site. (Dashed lines) The places in configuration space which are not occupied by the bosons during their evolution.

HCBM introduced in Chapter 2:

$$H = -J \sum_{\langle ij \rangle} (\hat{b}_i^\dagger \hat{b}_j + h.c.) + V_1 \sum_{\langle ij \rangle} \hat{n}_i \hat{n}_j + V_2 \sum_{\langle\langle ij \rangle\rangle} \hat{n}_i \hat{n}_j - \sum_i \mu_i \hat{n}_i \tag{3.27}$$

At this stage, we can assign the physical meaning of the terms in (3.27) as we described for the HCBM. The Hamiltonian can be separated into two parts $H = K + U$ in which $K = -J \sum_{<ij>} (\hat{b}_i^\dagger \hat{b}_j + h.c.)$ and $U = V_1 \sum_{\langle ij \rangle} \hat{n}_i \hat{n}_j + V_2 \sum_{\langle\langle ij \rangle\rangle} \hat{n}_i \hat{n}_j - \sum_i \mu_i \hat{n}_i$. Therefore, the path integral form of the partition function is:

$$Z = \sum_{L=0}^{\infty} \int_0^\beta d\tau_1 \ldots \int_{\tau_{L-1}}^\beta d\tau_L \sum_{i_{CP}(\tau)} W_L[i_{CP}(\tau)] \tag{3.28}$$

where the configuration weight is:

$$\begin{aligned} W_L[i_{CP}(\tau)] &= J^L \text{exp} \left\{ - \sum_{i=1}^{L} \int_{\tau_{i-1}}^{\tau_i} U(\tau) \right\} \\ &\equiv W(K_s, \xi_K; x_1, \ldots, x_K; y) \end{aligned} \tag{3.29}$$

with, $U(\tau) = V_1 \sum_{<ij>} \hat{n}_{i(\tau)}\hat{n}_{j(\tau)} + V_2 \sum_{<<ij>>} \hat{n}_{i(\tau)}\hat{n}_{j(\tau)} - \sum_j \mu_j \hat{n}_{j(\tau)}$. Here, the weight $W(K_s, \xi_K; x_1, \ldots, x_K; y)$ in (3.29) is written in a diagrammatic series in which K_s is the number of transitions between two nearest neighbour lattice sites, or the "kinks" in the lattice path integral; x_i are imaginary times at these transitions, ξ_K is the locations in space for all kinks as well as their direction, and the initial occupation numbers on all lattice sites; y stands for the Hamiltonian parameters. Fig. 3.4 illustrates an example of the evolution in the space-time configuration of a one dimensional system with 6 sites and 3 hardcore bosons, which can be called the "diagrams" after Feynman [55]. The graph visualizes the partition function, hence the condition $\alpha(\tau = 0) = \alpha(\tau = \beta)$ (arising from the *trace* in the calculation of partition function) has to be satisfied. As a result, the state at $\tau = 0$ must be the same as the state at $\tau = \beta$.

3.2.4 Diagrammatic Monte Carlo and worm algorithm

It is straightforward to employ the above outlined Monte Carlo technique, for example using the weight distribution (3.29), to transform between configurations. This can be implemented using two kinds of updates: A-type, which traverses the series index K_s (e.g. the number of hopping processes) and $B-$type, which changes the value of the series index K_s. Considering the diagrams of the partition function of the HCBM (3.28) illustrated in Fig. 3.4, we may suggest three updates as follow: a shift in imaginary time (time-shift) which is an A-type update; a kink-antikink creation and a kink-antikink annihilation which belongs to the $B-$type update. We should note that the occupation number for a given site is either 0 or 1 due to the hardcore constraint.

Time-shift (A-Type): Fig. 3.5 illustrates an example of a time-shift update. One randomly selects any kink in the space-time configuration and proposes a change (a shift) in imaginary time. This update does not change the nature of the other kinks in the configuration space as long as it can be placed anywhere between two nearest neighbour kinks. Let us assume that the selected kink is at time τ_k which describes the hopping process from site i to site $i + 1$. In other words, it just shifts the position of the selected kink and changes only the occupation number on site i from $n_2 = 1$ to $n_4 = n_2 - 1 = 0$ as well as the occupation number on site $i + 1$ from $n_1 = 0$ to $n_3 = n_1 + 1 = 0$. The left hand side

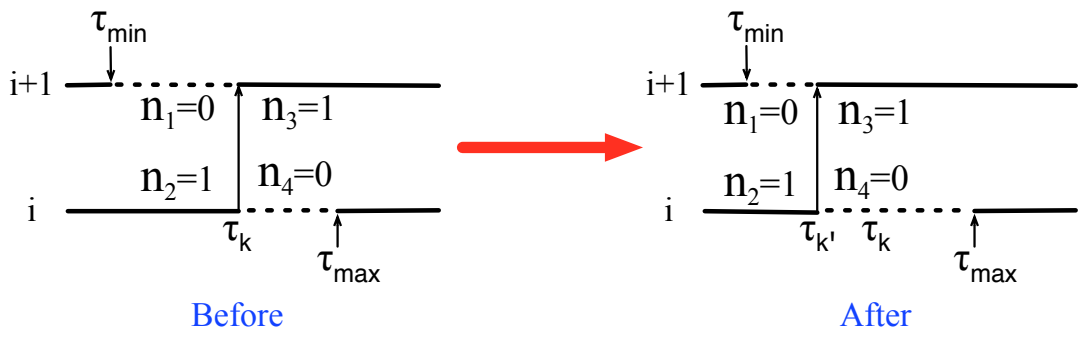

Figure 3.5: An example of a time shift update as described in the text.

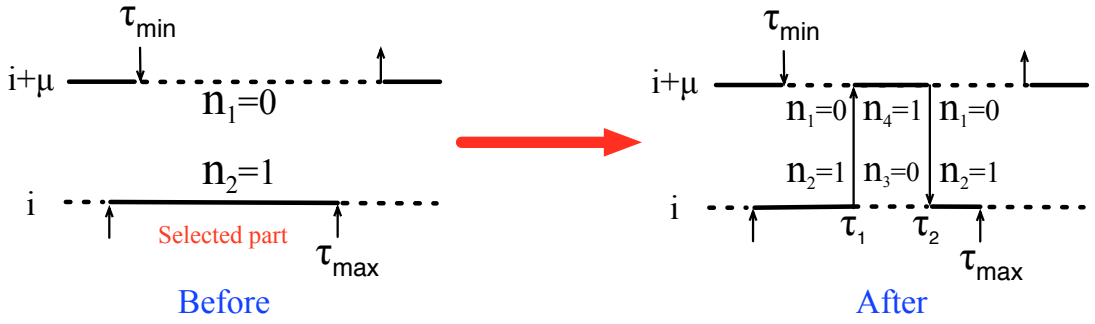

Figure 3.6: An example of a kink-antikink creation and annihilation update as described in the text.

shows the local configuration before the update whereas the right hand side is the local configuration after the update. There is no other change in the space-time configuration except at sites i and $i+1$, where $n^{'}_{i+1} = n_1, n^{'}_{i} = n_2$, and $n_{i+1} = n_3, n_i = n_4$. As a requirement for this update, the new position for this kink can be anywhere between τ_{min} and τ_{max} which are the times corresponding to the nearest neighbour kinks. Hence, we may propose the new position for this kink at $\tau^{'}_{k}$:

$$\tau^{'}_{k} = \tau_{min} + r \times (\tau_{max} - \tau_{min}) \tag{3.30}$$

where r is a random number which can be generated using the simple uniform random distribution.

Kink-antikink creation and annihilation (B-Type): The diagram in Fig. 3.6 shows an example of the kink-antikink creation update. We are interested in the flat trajectory parts of the configuration space where there is no kink. We propose an update by creating a

kink-antikink pair. In the left hand side of the diagram is the local configuration before the update and on the right hand side is the local configuration after the update. Let us assume that the total number of flat parts in the configuration space before the update is $N_i \leq 2K_s$ where K_s is the total number of the kinks. Therefore, the total number of flat parts is $N_i^{'} > N_i$ in the configuration space after the update. We can simply select a flat part randomly from all the flat parts N_i as: $r \times N_i + 1$ and direction with which the hopping transition will occur as: $\hat{v} = r \times d + 1$, where r is a random uniform distribution, and d is the dimension of the system. Finally, we need to choose the imaginary time boundaries in which we place a new kink-antikink pair: $\tau_1 = \tau_{min} + r \times (\tau_{max} - \tau_{min})$ and $\tau_2 = \tau_{min} + r \times (\tau_{max} - \tau_{min})$. The condition $\tau_1 < \tau_2$ is assumed. As a result, the changes in the occupation numbers are $n_3 = n_2 - 1$ and $n_4 = n_1 + 1$.

The kink-antikink annihilation, which removes the kink-antikink pair, can be established by selecting the flat part randomly, $r \times N_i^{'} + 1$, and it is the reverse step of the kink-antikink creation. However, we have to ensure that its imaginary time boundaries belong to the kink-antikink pair and that the kink-antikink pair annihilation process does not interfere with other kinks. The detailed balance condition reads:

$$\frac{1}{N_i} p(\tau_1, \tau_2)(d\tau)^2 W_\nu (d\tau)^{K_s} P^a(\nu \to \nu^{'}) = \frac{1}{N_i^{'}} p(\tau_1, \tau_2)(d\tau)^2 W_{\nu,} (d\tau)^{K_s} P^a(\nu^{'} \to \nu) \tag{3.31}$$

where P^a is the acceptance probability of the update, W is the weight function; and $p(\tau_1, \tau_2)$ is the uniform distribution, e. g., $p(\tau_1, \tau_2) = 2/(\tau_{max} - \tau_{min})^2$.

Estimators: It is straightforward to calculate the estimators for the potential energy as well as the kinetic energy in the context of the lattice path integral diagram discussed above. The calculation of the estimator for the potential energy is self-consistent [53]:

$$U_\nu = \beta^{-1} \int d\tau \sum_{jj^{'}} V_{jj'} n_j(\tau) n_j^{'}(\tau) \tag{3.32}$$

and the estimator for the kinetic energy is [53]:

$$T = -\frac{\langle K_s \rangle}{\beta} \tag{3.33}$$

Another quantity, namely the winding number [56], which is relevant to the superfluid density, is important to calculate. Unfortunately, we are not able to evaluate this quantity

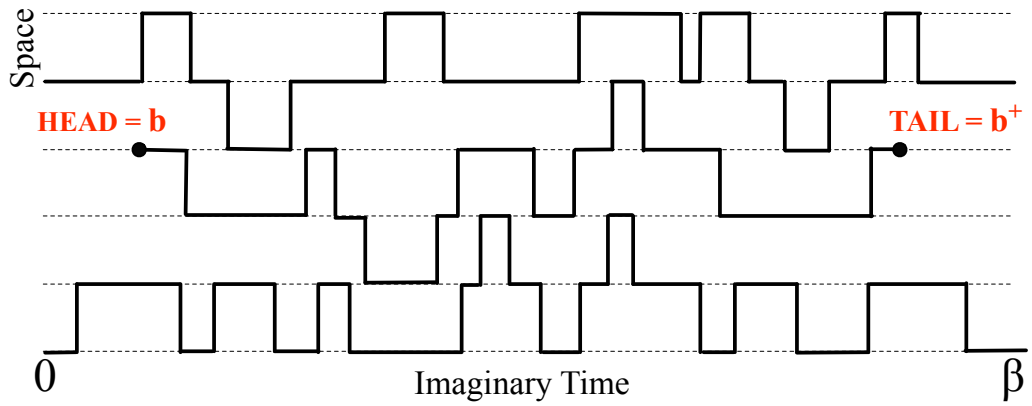

Figure 3.7: An example state within the extended configuration space: (Solid lines) trajectories of two closed world-lines and one opened world-line with two worm ends. Worm head and worm tail are marked by the solid circles. (Dashed line) The places in configuration space which are not occupied by the particles during their evolution.

using the above local update scheme (in principle, we are able to do it but it is impossible in the thermodynamic limit), therefore we must turn to the *worm algorithm*.

Worm sampling

The configuration space of the partition function Z contains only the closed paths (close trajectories), namely the $Z-$sector. The worm algorithm works in an extended configuration space as shown in Fig. 3.7, namely the G-sector, where one opens an extra world-line fragment called the "worm" in addition to closed world-line paths.

The worm algorithm is a local update algorithm but also has non-local changes, stepping beyond conventionally local update Metropolis schemes. It can overcome the problem of critical slowing down at a second order phase transition [57]. In the world-line representation, this algorithm creates two world-line discontinuities, and moves them around using local updates. Formally, this is done by simply adding the worm operators into the Hamiltonian (3.27), which has a new term given by:

$$H_{\text{worm}} \quad = \quad H - \alpha \sum_i (W_i^+ + W_i^-) \tag{3.34}$$

where, H is the original Hamiltonian (3.27), $W_i^{+(-)}$ is the worm head (tail) operator. This extra term allows the world-lines to be broken with a matrix element proportional to α.

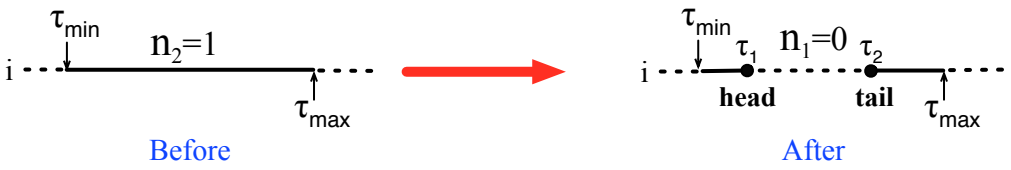

Figure 3.8: An example of a worm creation update as described in the text.

As a result, the decomposition of the partition function is embedded in the $G-$sector:

$$Z_e = \mathrm{Tr}\left\langle \mathcal{T}((\hat{b}_i(0)\hat{b}_j^\dagger(\tau) + \mathrm{h.c})\exp(-\beta H))\right\rangle \tag{3.35}$$

where $\mathcal{T}$ is the time ordering operator, and the term $(\hat{b}_i(0)\hat{b}_j^\dagger(\tau)+\mathrm{h.c})$ represents the worm operators [54]. We can perform an update within the worm algorithm as follows: a worm is created by inserting a pair of worm operators $W_i^{+(-)}$. The worm head can be creating or annihilating, depending on the choice of W. In principle, both ends can move randomly in space-time configuration, using local Metropolis or heat bath updates. However, we choose to move the worm head and fix the worm tail to simplify our simulation without any loss of generality. As a matter of fact, the worm head can wind around the lattice in both the temporal as well as spatial directions, a situation which results in a non-zero the winding number. After several updates, the worm head "bites" its tail and the discontinuities are removed, completing the update. A tremendous advantage of the worm algorithm is that it remains efficient in the presence of an external field [15, 16]. Another advantage of the worm algorithm is that it provides us with the ability to calculate the single particle propagator (Green's function) in imaginary time:

$$G(j,\Delta\tau) = \langle \hat{b}_{i+j}(\tau+\Delta\tau)\hat{b}_i^\dagger(\tau)\rangle \tag{3.36}$$

where $\hat{b}_i^\dagger(\tau)$ is the creation operator which creates a boson on site i and at imaginary time τ, and $\hat{b}_{i+j}(\tau+\Delta\tau)$ is the annihilation operator which destroys a particle on site $i+j$ at time $\tau+\Delta\tau$.

There are four types of updates in the worm algorithm, namely: worm creation, worm annihilation, worm time shift, and worm space shift.

Worm creation: This type of update switches the configuration space from the $Z-$sector to the $G-$sector, therefore we can only propose this update in $Z-$sector. We select randomly a flat path in the configuration space and place the worm head at imaginary time

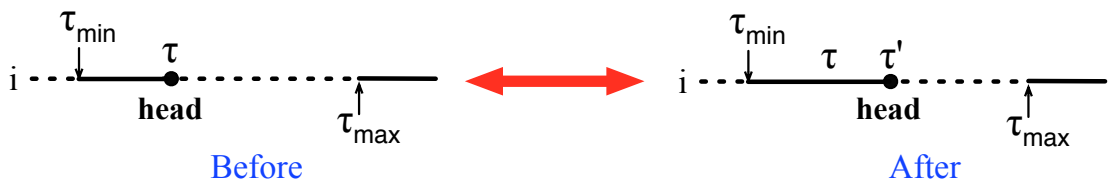

Figure 3.9: An example of a worm time shift update as described in the text.

$\tau_1 = \tau_{min} + r \times (\tau_{max} - \tau_{min})$ and the worm tail at time $\tau_2 = \tau_{min} + r \times (\tau_{max} - \tau_{min})$. Fig. 3.8 shows the local configuration before the creation of the worm on the left hand side of the diagram, whereas the two possible local configurations after the creation of worm are shown on the right hand side.

Worm annihilation: This type of update switches the configuration space from the $G-$sector to the $Z-$sector, and therefore it only works as long as we are initially in the $G-$sector. This update is the reverse procedure of worm creation. We should note that we are able to remove the worm if it appears in the selected flat interval. As a result, this update is accepted with some probability p_a, and the detailed balance for worm creation and worm annihilation updates reads:

$$C_\nu \frac{1}{N_i} W_\nu (\tau_{max} - \tau_{min})^2 P_c^{(a)} = C_{\nu'} p_a \omega_G W_{\nu'} P_a^{(a)} \tag{3.37}$$

where $P_c^{(a)}$ is the acceptance probability of worm creation update; $P_a^{(a)}$ is the acceptance probability of worm annihilation; ω_G is a free parameter $\sim \langle \frac{1}{N_i} \rangle$; and the rest follows the conventional notation.

Time shift: this update is the same as the kink shift in imaginary time update discussed above. In this update, the worm head can either advance or recede in time as illustrated in Fig. 3.9.

Space shift: we propose this update to create/annihilate a kink either to the left or to the right of the worm head. Similar to the time shift, this update is accepted with some probability p_s as well. We illustrate this type of update in Fig. 3.10.

In addition to the original worm algorithm [15, 16] in which worm does not have a direction (just a random walk through a configuration space), recently introduced improvements in this algorithm use the locally optimal worm updates with which a "directed"

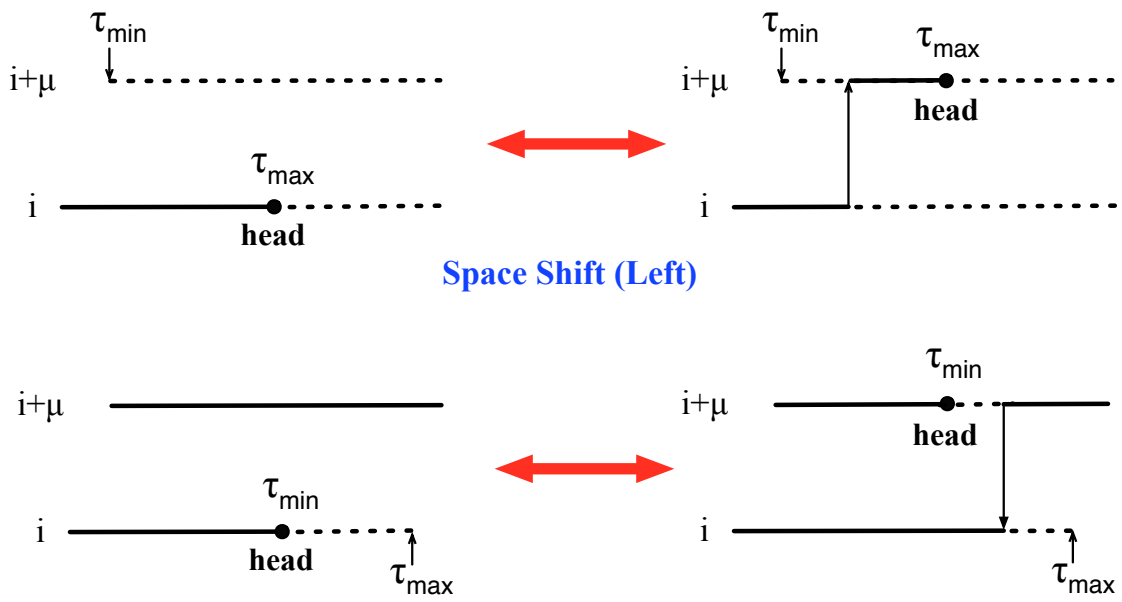

Figure 3.10: An example of the worm space shift update as described in the text. (Upper panel) Worm shifts in space to the left. (Lower panel) Worm shifts in space to the right.

worm is introduced. The main idea is to incorporate the best of two approaches, namely the directed loop algorithm [51, 52] and "locally optimal Monte Carlo," [54] into the worm algorithm. As Pollet *et. al.* suggest, the greatest advantage of "locally optimal Monte Carlo" is the possibility of assigning a direction to the worm head after passing a kink. On the other hand, the great advantage of the directed loop algorithm is in how a worm passes and modifies a kink. As a result, a "directed" worm can move more efficiently in configuration space.

Throughout this dissertation, we will use the worm algorithm with this improvement in the update scheme. Therefore, we will describe these updates in more detail in the following:

1. We select randomly a position in the configuration space of $Z-$sector at site i and imaginary time τ (i, τ). Let us assume that we know all occupation numbers at time τ, and we will propose a direction of the worm to the left or the right with equal probability and we continue assuming that the worm head moves to the right.

2. The worm-pair (including the worm head and worm tail) is created at (i, τ). If the occupation number at this position is different from zero, e.g. occupation number $n = 1$, we insert the worm pair or go back to step 1 with equal probability. If the occupation number is zero (n = 0), then a worm is inserted with probability 50% (without the loss of generality). As soon as the worm-pair is created, we switch from the $Z-$sector to the $G-$sector and the worm propagates in the $G-$sector.

3. Let us assume the energy to the left (right) of the worm head is E, so that the imaginary time shift is proposed as $\Delta\tau = p/E = -\ln(u)/E$, where u is drawn from a random uniform distribution within an interval $0 < u < 1$. Therefore, the new time position of the worm head is $\tau^{'} = \tau + \Delta\tau$

4. As soon as the worm head meets its tail during its propagation, we remove the worm-pair with probability one. In other words, we switch from the $G-$sector with one open trajectory to the $Z-$sector with all closed trajectories.

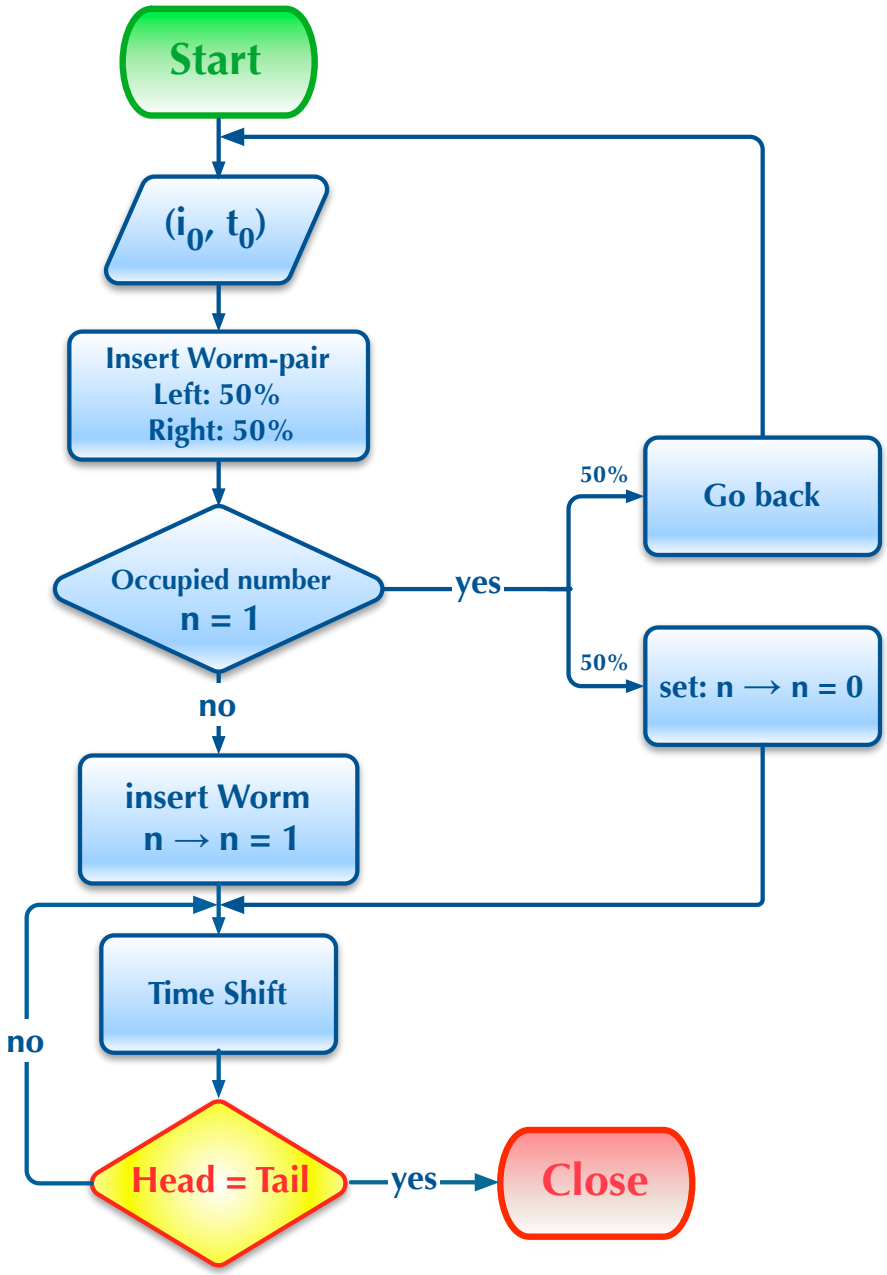

Figure 3.11: A flowchart of the locally worm algorithm optimal update.

5. In the case where the new worm time is greater than the time to the next interaction, the new worm time is assigned to be equal to the time of the next kink. The worm can bounce back, pass, annihilate or modify the kink following the detailed balance equation.

6. If no kink is encountered in the imaginary time shift interval, we create a kink, or the worm can bounce back.

7. Go back to step 3.

The flowchart in Fig. 3.11 illustrates the algorithm described above. The winding number is the number of times which the worm head winds around the system before meeting the worm tail. The superfluid density (stiffness) ρ_S can be evaluated in terms of the winding number [56]:

$$\rho_S = \frac{\langle M^2 \rangle L^{2-d}}{\beta d} \tag{3.38}$$

where $\langle \ldots \rangle$ is an average, M is the total winding number, and L is the linear size of the system. There is another important observable which can be measured as well: the static structure factor at the wave vector $\mathbf{Q}$ ($S(\mathbf{Q})$) reads:

$$S(\mathbf{Q}) = \frac{1}{N^2} \left\langle \left| \sum_{i=1}^{N} \hat{n}_i e^{i\mathbf{Q}.\mathbf{r_i}} \right|^2 \right\rangle \tag{3.39}$$

where, $N = L \times L$ is the number of lattice sites for 2D systems. These useful quantities help us characterize the different phases exhibited in the systems which we will study.

3.3 Equilibrium problem and statistical error estimators

When we perform a Monte Carlo simulation, several technical issues are immediately presented, including the problem of identifying when a system is in equilibrium, and the estimation of error bars.

3.3.1 Equilibrium problem

Starting a Monte Carlo simulation from an arbitrary configuration will take a number of MC steps (sometimes referred to in terms of something akin to a thermalization time, t_{therm}) to reach a state of thermal equilibrium after which collected data is meaningful. However, there is no mathematical relation for the thermalization time t_{therm} in terms of the characteristic time t_0 [53] since the latter is a quantity characterized in the equilibrium state, whereas the former depends on states far from the equilibrium. In practice, one can look at the convergence properties of the statistical error bars to ascertain when a sufficient number of MC updates has been taken. For example, if we are in equilibrium after N-MC updates, it must be true that the statistical error bars after 2N-MC updates will be of the same magnitude. All data collected after N-MC updates can then be included in the calculation of meaningful averages.

3.3.2 The statistical error estimators

There are two classes of errors in Monte Carlo simulations, namely: *statistical errors* and *systematic errors*. The latter are due to the procedures which we have used to measure expectation values, and therefore its effects will persist regardless of how we perform MC sampling. On the other hand, statistical errors are due to random changes in the simulation quantities from measurement to measurement, and may be estimated simply by taking many measurements of a quantity in which we are interested, and then evaluating the spread of these values.

We consider the thermal average of a physical observable A, calculated as a mean of its values over a large set of N_s samples $\{A_i\}$ generated by our sampling procedure, we have:

$$\langle A \rangle \approx \frac{1}{N_s} \sum_{i=1}^{N_s} A_i. \tag{3.40}$$

If we also assume that the calculation of A takes place for values of A_i such that the measurements are independent and normally distributed (in order to meet the condition for the central limit theorem [58]), we can estimate the uncertainty of $\langle A \rangle$ as:

$$\sigma \approx \sqrt{\frac{1}{(N_s-1)}\sum_{i}^{N_S}(A_i - \langle A\rangle)^2}. \tag{3.41}$$

However, we sample states via a Markov chain in which each state is generated starting from the previous state. Sequential states in this random walk are thus correlated, and we underestimate the statistical error by using (3.41). One must find a way to perform the average over uncorrelated configurations.

The common approach is to split the simulation up into a number of equal blocks containing a large number (thousands) of sequential configurations, over which partial averages for each block are calculated and stored. One then constructs bins with a fixed number of data blocks in each, and obtains the error as the standard deviation (variance) of the resulting histogram. We now discuss this procedure in more detail following the lecture set by N. Prokof'ev [53]:

Starting from an initial configuration, let us assume that a simulation result after a time t_0 is:

$$\langle A\rangle_{0,t_0} = \langle A\rangle_{\text{exact}} + \delta A_{t_0} \tag{3.42}$$

where $\langle \ldots \rangle$ stands for the average. As a matter of fact, we need to sample only a very small fraction of relevant configurations to obtain accurate results in the "importance sampling" algorithm [59]. This feature is a significant advantage of Monte Carlo techniques, and arises because the value of a quantity A in a configuration ν (A_ν) is insensitive to the detailed structure of the configuration ν. Hence, a number of different configurations result in a value A that is the same or close to A_ν. If t_0 is large enough, we in principle can assume that we have a reasonably good sampling of the relevant region in configuration space. Now, let us double the calculation time and calculate $\langle A\rangle_{t_0,t_0+t_0}$ over configurations generated in the interval simulation time $[t_0, t_0+t_0]$. The simulation result in (3.42) becomes:

$$\langle A\rangle_{t_0,t_0+t_0} = \langle A\rangle_{exact} + \delta A_{t_0,t_0+t_0} \tag{3.43}$$

We repeat this procedure a number of times. As a result, we obtain a set of independent random variables called "block averages" with the same average $\langle A\rangle_{exact}$ and standard

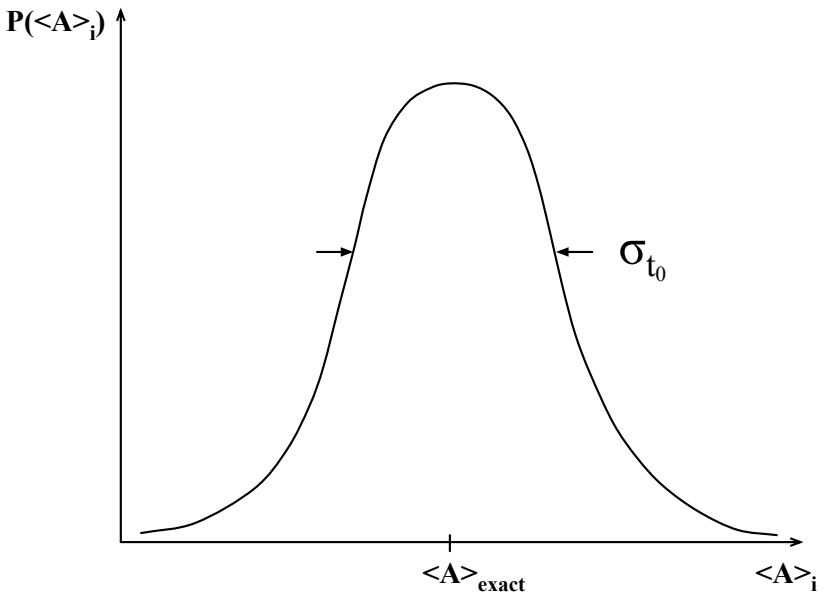

Figure 3.12: An example of Gaussian distribution of block averages $\langle A_i \rangle$ centered at $\langle A \rangle_{exact}$ and the width or the standard deviation σ_{t_0} marked by the arrows.

deviation σ_{t_0}. The average over the entire simulation time ($t = Nt_0$, $N \neq N_s$) is evaluated by the central limit theorem:

$$\langle A \rangle_{0,t} = \langle A \rangle = \frac{\sum_{i=1}^{N} \langle A \rangle_i}{N} \tag{3.44}$$

which has a smaller standard deviation and its distribution is Gaussian:

$$\begin{aligned} \sigma_t^2 &= \frac{1}{N^2} \sum_{i=1}^{N} \sigma_{t_0}^2 \\ &= \frac{t_0}{t} \sigma_{t_0}^2 \end{aligned} \tag{3.45}$$

Fig. 3.12 illustrates an example of a Gaussian distribution of $\langle A \rangle_i$. As we see, the standard deviation σ_t in (3.45) scales as $t^{-1/2}$. In other words, the longer the simulation time is, the more accurate the results become. Moreover, one is able to calculate the statistical error obtained in Monte Carlo simulations by using the definition of σ_t as the dispersion of block-averages:

$$\sigma_t = \sqrt{\frac{\sum_{i=1}^{N} (\langle A \rangle_i - \langle A \rangle)^2}{N^2}} \tag{3.46}$$

In order to obtain formula (3.46), we have assumed that the simulation time is long enough, meaning that $\langle A\rangle_i$ are statistically independent regardless of the (unknown) parameter t_0. If $\langle A\rangle_i$ are also strongly correlated, then our analysis is no longer meaningful. In order to avoid this problem, one has to use different methods, e.g. blocking, bootstrapping, or jackknife methods. The main idea of these methods, which are discussed below, is to make the averaged blocks larger.

In the *blocking method*, we consider the list of block numerators $(S_1, S_2, \ldots, S_N)$ with each block containing N_A accepted configurations, $S_i = \sum_{\nu\in\ i^{th}block} A_\nu$, instead of evaluating the error bar with the list of block averages $(\langle A\rangle_1, \langle A\rangle_2, \ldots, \langle A\rangle_N)$. By definition, $\langle A\rangle_i = S_i/N_A$, and we have to calculate not only the error bar $\sigma_t^{(N)}$ in (3.45) but also $\sigma_t^{(M)}$ for the smaller number M of larger blocks. Under the constraint $N = M\times j$, we can form a "superblock" from j blocks:

$$\langle B\rangle_i = \frac{1}{j\times N_A}\sum_{k=1+(i-1)\times j}^{i\times j} S_k \tag{3.47}$$

As a result, the error bar for smaller number M of larger blocks $\sigma_t^{(M)}$ reads:

$$\sigma_t^{(M)} = \frac{1}{M}\sqrt{\sum_{i=1}^{M}(\langle B\rangle_i - \langle A\rangle)^2} \tag{3.48}$$

Another idea for making larger superblocks is to combine N blocks selected randomly from the set $\{S_i\}$. This method is called *bootstrapping method*. In this method, the values in the set may contribute to the superblock more than once. A significant advantage of the bootstrap method is that its error bar does not depend on the choice of t_0 for the prime block [53].

Finally, in the *jackknife method*, one forms the superblocks by combining all except one block:

$$\langle B\rangle_i = \frac{1}{(N-1)\times N_A}\sum_{k\neq i}^{N} S_k \tag{3.49}$$

The jackknife method is often used in the case where the measurement has the form $F = \langle X\rangle/\langle Y\rangle$, for which it becomes difficult to calculate the error propagation and correlations [60].

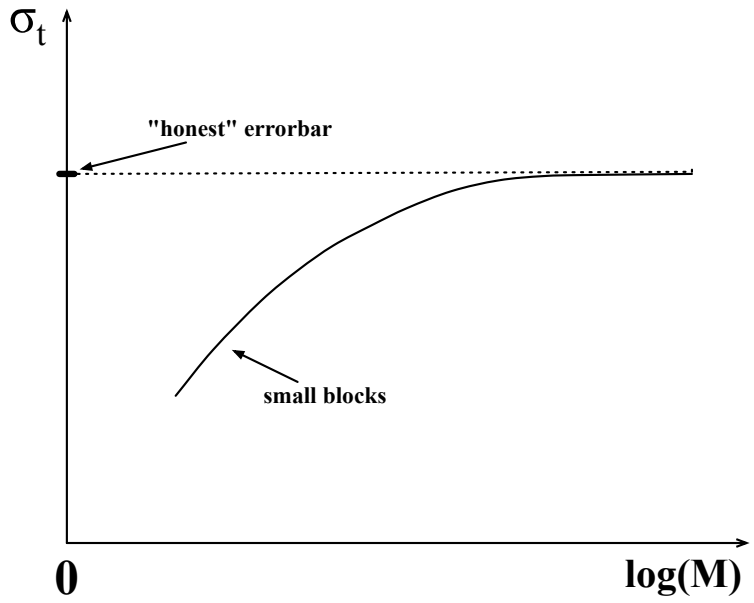

Figure 3.13: An example of how the error bar σ_t depends on the number of blocks M. The dashed line marks an "honest" error bar. The solid line is the asymptote of the error bar σ_t versus the number of blocks M. When the number of blocks M is small, the deviation of this function from the "honest" error bar is large, whereas it approaches the "honest" error bar for large number of blocks.

Regardless of which way we estimate statistical errors, we must obtain the "honest" error bar (3.45) in the limit of long time simulations as shown in Fig. 3.13.

Chapter 4

Results and discussions

In this chapter, we will present our studies on the interplay between superfluidity and localization in which the HCBM (discussed in Chapter 2) exhibits unconventional superfluidity arising from different sources of localization. We have used QMC-the worm algorithm in the lattice path-integral representation [15, 16] with the specific implementation given by locally optimal worm updates [54] (discussed in Chapter 3). We first discuss the vacancy-based supersolid near localization, which is induced by interactions, within the context of the repulsive interaction "$V_1 - V_2$" model, and in the absence of any external potential. Secondly, we discuss another supersolid near localization induced by an external periodic potential, within the context of the repulsive interaction "V_1" model. Finally, we provide an example of disorder-induced superfluidity, which does not occur in the absence of disorder, within the context of the *attractive* interaction "V_1" model.

4.1 Vacancy-based supersolidity

4.1.1 The repulsive interaction $V_1 - V_2$ model

In this work, our starting point is the $V_1 - V_2$ model introduced in Chapter 2, section 2.2:

$$H = -J \sum_{\langle ij \rangle} (\hat{b}_i^\dagger \hat{b}_j + h.c.) + V_1 \sum_{<ij>} \hat{n}_i \hat{n}_j + V_2 \sum_{<<ij>>} \hat{n}_i \hat{n}_j - \mu \sum_i \hat{n}_i \qquad (4.1)$$

The first term of (4.1) describes the process of a particle hopping to a nearest-neighbour site which contributes to the kinetic energy. As mentioned in Chapter 2, we remind the

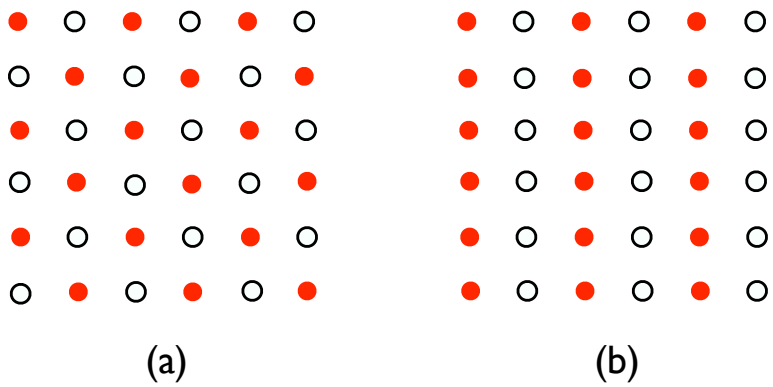

Figure 4.1: Classical crystal phases at half-filling on the square lattice. Filled circles represent particles, empty circles empty sites. (a) The checkerboard crystal as the ground state if $V_1 \gg V_2$, (b) The striped crystal as the ground state if $V_1 \ll V_2$

reader that we set the hopping amplitude to be the unit of energy scale (i.e. $J = 1$). The second and third terms represent repulsive interactions between bosons on nearest and next-nearest neighbour sites, respectively. The last term is the chemical potential which determines the number of bosons N_B.

Previous studies [18, 19] of the ground state of (4.1) have yielded evidence of three possible phases at half-filling ($\rho = 0.5$): a superfluid, a checkerboard crystal and a striped crystal. The competition between the nearest neighbour interaction V_1 and the next nearest neighbour interaction V_2 promotes the formation of the latter two phases. In the regime at which the nearest neighbour interaction V_1 dominates, e.g. $V_1 \gg V_2$, the crystal is a checkerboard where the sites are alternately occupied and empty (see Fig. 4.1a). On the other hand, in the regime in which the next nearest neighbour interaction V_2 dominates, e.g. $V_2 \gg V_1$, the crystal is striped, that is, composed of horizontal (or vertical) lines of sites alternately occupied (see Fig. 4.1b).

Doping the striped crystal away from half filling yields a supersolid phase, whereas a first-order quantum phase transition separates the checkerboard crystal from a superfluid [18, 19]. For a sufficiently strong next-nearest neighbour repulsion, the Hamiltonian (4.1) also features a commensurate crystal phase at quarter filling which we sometimes refer to as "star" crystals (shown in Fig. 4.2). We should note that the Hamiltonian (4.1) has particle-hole symmetry, and thus the phase diagram between half and full fillings is the

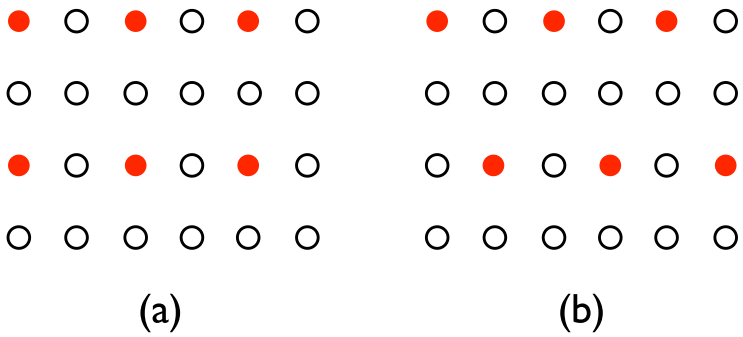

Figure 4.2: Classical, degenerate star crystal phases at quarter-filling on the square lattice. Filled circles represent particles, empty circles empty sites. Quantum fluctuations lift the degeneracy, selecting (a) as the ground state if $V_1 < 2V_2$, (b) otherwise

specular reflection of that between zero and half filling. It has also been shown that a supersolid phase can occur, upon doping the star solid above quarter-filling [20].

Here, we systematically investigate the ground state phase diagram of (4.1) which we establish by extrapolating the Monte Carlo results at low temperature. In order to characterize the various phases, we computed the superfluid fraction ρ_S using the well-known winding number estimator (3.38), as well as the static structure factor, introduced in Chapter 3. The presence of crystalline long-range order is signaled by a finite value of S(**Q**) for some specific wave vectors, in the thermodynamic limit. In particular, **Q** = (π, π) is the wave vector associated to checkerboard order at half filling, whereas **Q** = $(\pi, 0), (0, \pi)$ signals striped order at half filling, as well as star order at quarter-filling.

4.1.2 The results

Fig. 4.3 summarizes our results for the ground state phase diagram of (4.1). Three distinct phase boundaries are identified. The first one (open circles) separates a superfluid from a star crystal at quarter filling. In this work, we focus our attention on the region above the open circles, i.e., wherein a star crystal exists. The other two phase boundaries refer to the behaviour of the system at half-filling, separating a stripe crystal (filled boxes) [checkerboard crystal (filled circles)] from a superfluid. We will now discuss the physical behaviour at other densities as a function of V_1 and V_2.

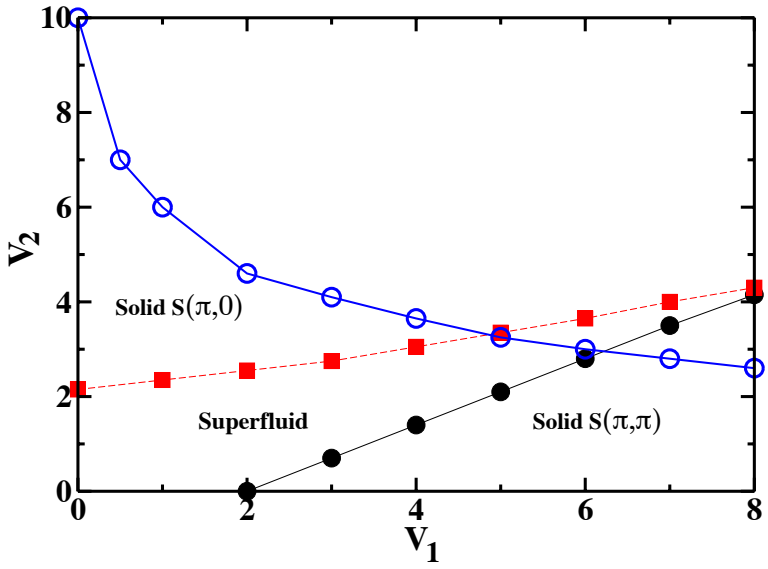

Figure 4.3: Ground state phase diagram of (4.1). Lines are guides to the eye. Symbols lie at computed phase boundaries, namely between (a) a "star" crystal and a superfluid (below open circles) at $\rho = 0.25$ (open circles) (b) a "striped" $(\pi, 0), (0, \pi)$ crystal and a superfluid (below the filled boxes and above filled circles) at $\rho = 0.5$ (filled boxes) and (c) a superfluid (below the filled boxes and above filled circles) and a "checkerboard" crystal (filled circles), also at $\rho = 0.5$. Statistical errors are smaller than symbol sizes. Results at $\rho = 0.5$ are consistent with previous works.

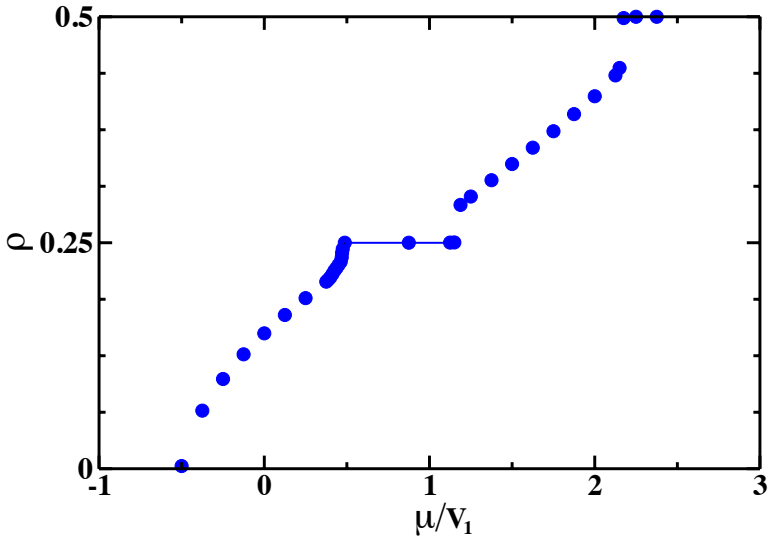

Figure 4.4: Density ρ versus chemical potential μ for V_1 = 8, V_2 = 3.5. Statistical errors are smaller than symbol sizes. A first-order quantum phase transition separates the "star" crystal at $\rho = 0.25$ and the "checkerboard" crystal at ρ = 0.5 from a superfluid phase at intermediate densities. Results shown are for a square lattice with L = 24. A continuous phase transition to a vacancy supersolid occurs below ρ = 0.25

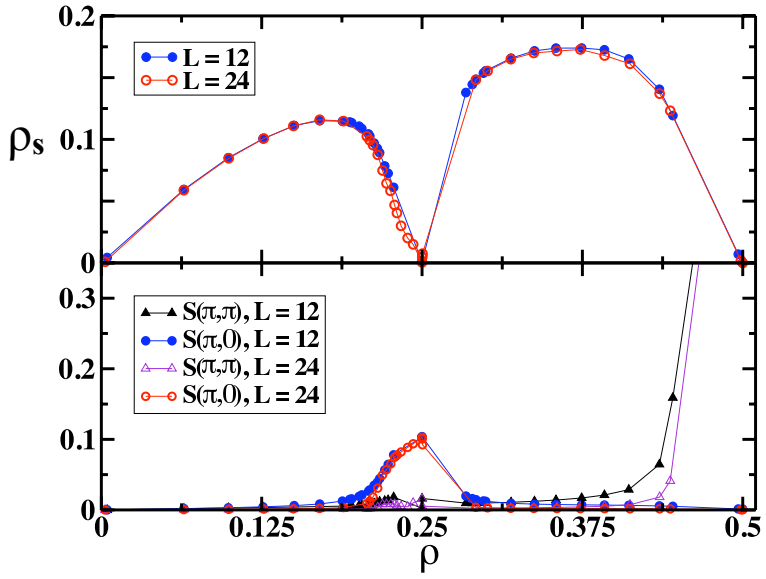

Figure 4.5: Superfluid density ρ_S (upper panel) and static structure factor S(**Q**) (lower panel) for V_1 = 8, V_2 = 3.5 for two system sizes and the two wave vectors **Q** = (π, π) and **Q** = $(\pi, 0), (0, \pi)$. Statistical errors are smaller than symbol sizes.

Fig. 4.4 shows the density computed as a function of the chemical potential for V_1 = 8, V_2 = 3.5. The ground state of the system is a checkerboard crystal at half filling. Density jumps signal first-order phase transitions above quarter- and below half-filling; everywhere else the curve is continuous albeit with a clear discontinuity of the first derivative (i.e., of the compressibility) on approaching ρ = 0.25 from below.

Fig. 4.5 displays the superfluid density as well as the static structure factor, computed for both $(\pi, 0)$ and $(0, \pi)$. The superfluid density is everywhere finite, except at commensurate values, whereas the static structure factor is finite at and near commensuration.

Based on these results, we conclude that the system is superfluid for $0.25 < \rho < 0.5$, with first-order quantum phase transitions to the star (checkerboard) crystal at ρ = 0.25 (ρ = 0.5). For $0 \leq \rho(\mu) \leq 0.25$, on the other hand, the system features two continuous phase transitions, one from a superfluid to a vacancy-based supersolid, corresponding to the change in slope of the $\rho(\mu)$ curve, and the other from the supersolid to the star crystal at ρ = 0.25. It is interesting to compare the results right above and below quarter filling (Fig. 4.5) in order to appreciate the effectiveness in distinguishing a homogeneous supersolid

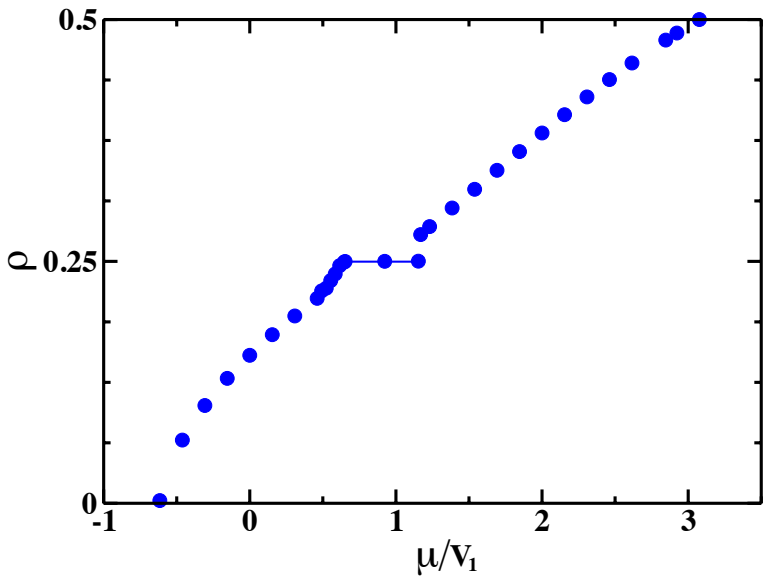

Figure 4.6: Density ρ versus chemical potential μ for V_1 = 6.5,V_2 = 3.5 and linear system size L = 24. Statistical errors are smaller than symbol sizes. A continuous quantum phase transition separates the star crystal from a supersolid on the vacancy side ($\rho < 0.25$), whereas a first order phase transition from the star crystal to a superfluid exists on the interstitial ($\rho > 0.25$) side.

phase from coexistence of two phases.

A similar scenario is observed for (V_1, V_2) pairs for which the ground state of the system at half-filling is superfluid, where the only difference is the absence of the crystalline phase at ρ = 0.5. In this case too, a vacancy-based supersolid exists below quarter-filling and a first-order phase transition separates the star crystal from a superfluid above quarter-filling. The superfluid phase extends all the way to half-filling as the competition between nearest-neighbour and next-nearest-neighbour interactions does not result in any crystal ordering. Results for one example in this region, i.e., V_1 = 6.5, V_2 = 3.5, are shown in Figs. 4.6 and 4.7. This behaviour should be contrasted to the one shown in Figs. 4.8 and 4.9 for the case $V_1 = V_2 = 5$. This parameter choice stabilizes a star crystal at quarter-filling and a stripe crystal at half-filling. A supersolid phase exists everywhere between the star and the stripe crystal. A vacancy rich supersolid phase occurs below filling 0.25, with a continuous phase transition to a superfluid at lower densities. A phase transition also occurs in this case above quarter filling, between a star and a striped supersolid; its location

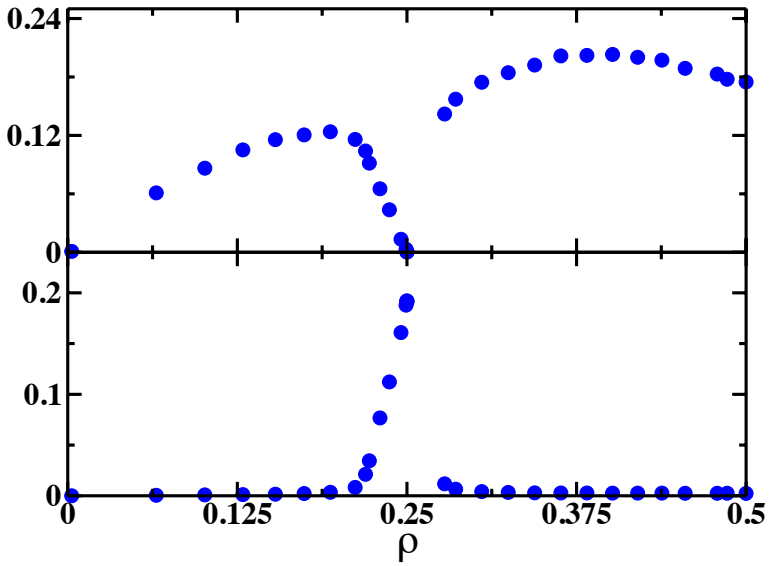

Figure 4.7: Superfluid density ρ_S (upper panel) and static structure factor S(**Q**) and **Q** = $(\pi, 0), (0, \pi)$) (lower panel) for V_1 = 6.5, V_2 = 3.5 for two system sizes. System size is L = 24. A supersolid phase exists only on the vacancy side below quarter-filling. The ground state of the system at half-filling is superfluid.

is signaled by a "kink in the numerical value of the static structure factor (Fig. 4.9, lower panel). This phase transition was claimed to be of first order in Ref. [20], based on a discontinuous jump in the value of the quantity $|S(\pi, 0) - S(0, \pi)|$ across the transition. If the values of V_1 and V_2 are such that a checkerboard crystal or a superfluid emerges at half-filling no supersolid phase intervenes in the $0.25 < \rho < 0.5$ interval.

The physical mechanism underlying the presence of a supersolid phase in this model away from commensurate fillings, even on lattices other than the square, is whether or not defects such as interstitials or vacancies can move without frustration. On the triangular lattice at filling $\rho = 1/3$, and in the presence of nearest-neighbour repulsion only, interstitial particles can freely hop around, hence Bose-condensing. At a finite concentration of vacancies, on the other hand, the system can lower its energy by forming a domain wall, i.e., vacancies phase separate [22, 23, 24, 25, 26]. The roles are reversed in our case, on the square lattice at quarter-filling. There is no cost in moving a vacancy around, in either the Fig. 4.2(a) or 4.2(b) scenarios, vacancies will thus condense. Conversely, the lowest energy needed to create an interstitial in the case of Fig. 4.2(b) (i.e., $V_1 > 2V_2$) is $4V_2$,

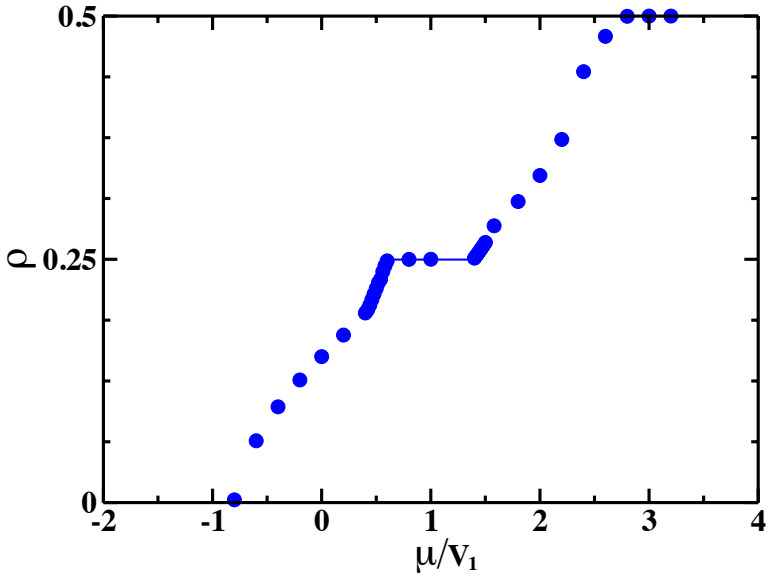

Figure 4.8: Density ρ versus chemical potential μ for V_1 = 5,V_2 = 5 and linear system size L = 24. Statistical errors are smaller than symbol sizes. Continuous quantum phase transitions separate both star and stripe crystals from supersolid phases on both sides. A continuous phase transition from a supersolid to a superfluid takes place below quarter-filling.

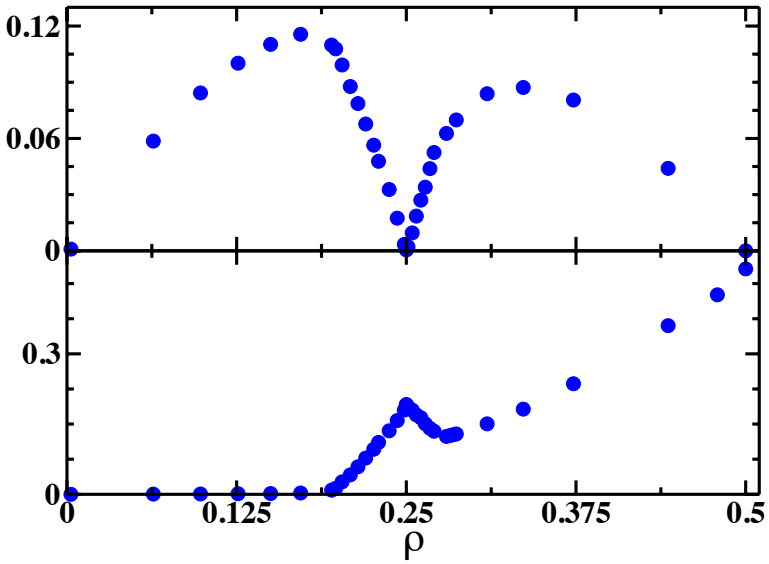

Figure 4.9: Superfluid density ρ_S (upper panel) and static structure factor S(**Q**) and **Q** = $(\pi, 0), (0, \pi)$ (lower panel) for V_1 = 5, V_2 = 5. System size is L = 24. A supersolid phase exists everywhere between quarter- and half-filling, and below quarter-filling.

which requires that a crystal atom also move to an empty row. The energy can only be lowered by higher order processes in term of J/V_1, which gives rise to the same domain wall argument invoked above for vacancies. This is the phase separation shown in Fig. 4.4.

The lowest energy needed to create an interstitial in the case shown in Fig. 4.2(a) (i.e., for $V_1 < 2V_2$) is $2V_1$, which corresponds to an interstitial between two crystal atoms. Those two crystal atoms can now hop around at no potential energy cost, which corresponds to the supersolidity seen in Fig. 4.8. This simple perturbative argument fails to account for the scenario of Fig. 4.6, as higher order processes renormalize the transition point. The same physical considerations also easily explain the lack of a supersolid phase of either vacancies or interstitials on the $kagomé$ or honeycomb lattices [61, 62].

In an optical lattice, interactions among nearest and next-nearest neighbouring atoms could arise from long-ranged (e.g., dipolar) interactions among particles. The ratio between V_1 and V_2 for polar molecules is $2\sqrt{2}$. The star solid, and the corresponding vacancy supersolid might thus be seen in experiment for $V_1 > 10$ (see Fig. 4.3) [63], albeit with rather strong requirements on the density and temperature. Observation of a super-

solid seems thus possible with existing techniques.

4.2 Supersolidity in a periodic superlattice

4.2.1 The *repulsive* interaction V_1 model

In this section, we study the repulsive interaction V_1 model (see Section 2.2):

$$H = -J \sum_{\langle ij \rangle} (\hat{a}_i^\dagger \hat{a}_j + h.c.) + V_1 \sum_{\langle ij \rangle} \hat{n}_i \hat{n}_j - \sum_i \mu_i \hat{n}_i \tag{4.2}$$

Here, we consider both triangular and square lattices of $N = L \times L$ sites, with periodic boundary conditions. The last term in (4.2) represents an external "pinning" potential, chosen as $\mu_i = \mu + \epsilon_i$, which is a site-dependent chemical potential. $\epsilon_i = -\epsilon$ if site i belongs to the pinning sublattice (see Fig. 4.11), and is zero otherwise. We note that $\epsilon > 0$, and is defined as the strength of the pinning potential.

For sufficiently strong nearest-neighbour repulsion, the ground state of the system is known to be a crystal, at particle density ρ = 1/2 ("checkerboard" solid) on a square lattice (Fig. 4.1a) and ρ = 1/3 (and 2/3) on a triangular lattice (Fig. 4.10). We include here a sublattice of *attractive* sites as well, acting as a strong pinning potential (see Fig. 4.11). The sublattice is purposefully chosen *not* to correspond to any crystal structure which the system forms in the absence of an external potential. For a sufficiently strong pinning potentials, additional crystalline phases can be expected to appear, registered with the adsorption sublattice; henceforth, we shall refer to these crystalline phases as *commensurate*. For example, our choice of pinning potential on the triangular lattice is such that particle density $\rho = \rho_C$ = 1/4 corresponds to a commensurate crystal, while $\rho = \rho_I$ = 1/3 corresponds to an incommensurate one. In other words, the terms "commensurate" and "incommensurate" are with respect to the pinning potential.

Films of ^{4}He adsorbed on strongly attractive substrates, such as graphite, have been the subject of intense experimental and theoretical investigation, motivated by the remarkable variety of phases that such films display [64, 65]. A decade ago, Crowell and Reppy first suggested the existence of a supersolid phase in the second layer of an adsorbed ^{4}He film on graphite [66, 67], but this contention has been recently brought back to fore [68].

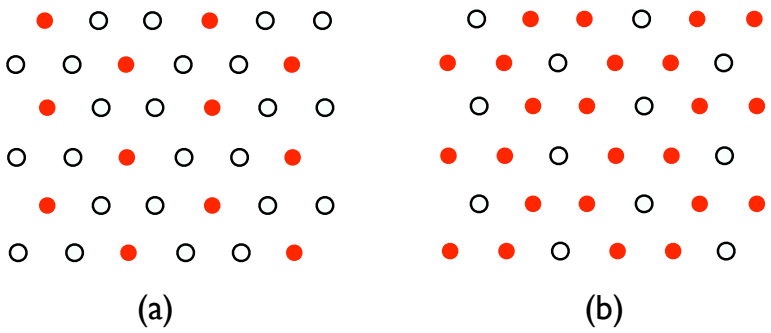

Figure 4.10: Classical crystal phases on a triangular lattice in the absence of any external potential and for sufficiently strong nearest-neighbor repulsion (a) at a density ρ = 1/3 and (b) at a density ρ = 2/3. Filled circles represent particles, empty circles empty sites.

In particular, it is suggested that a supersolid phase may occur in the vicinity of (or in correspondence with) a crystalline phase of the second adsorbed helium layer, *registered* with the underlying substrate. However, the most recent, first-principles numerical studies of helium films on graphite have yielded no evidence of such a supersolid phase, as no such registered crystal is observed [69].

That an external potential can significantly alter the phase diagram of a system of interacting bosons, giving rise to additional phases, is well known. For example, we have recently shown how a disordering potential can give rise to a glassy phase, as well as induce superfluidity in systems that do not otherwise display it [70].

Here, we investigate the possible existence of supersolid phases of many-boson systems in the vicinity of crystalline phases stabilized by external periodic potentials (such as that due to the adsorption sites of a corrugated substrate), i.e., *not* present in the phase diagram of the system in the absence of an external potential. Our study is based on a lattice model of interacting bosons, similar to that which has been utilized in previous theoretical works [71] as a minimal model of the very nearly two-dimensional (2D) first few ^{4}He adlayers on graphite [72, 73].

The results shown here correspond to a temperature T sufficiently low (typically $\beta = 1/T \approx L$), so as to be regarded sufficient to regard all obtained physical estimates to be representative of the absolute zero ground-state. With regard to the static structure factor, for the triangular lattice, $\mathbf{Q} = (\pi, 2\pi/\sqrt{3})$ is a wave vector corresponding to the registered (commensurate) crystal at $\rho = \rho_C$ = 1/4, while $\mathbf{Q} = (4\pi/3, 0)$ to an incommensurate

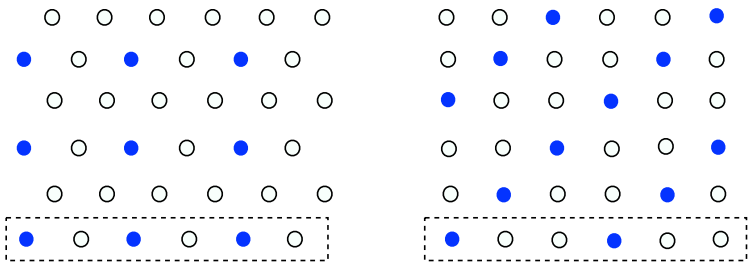

Figure 4.11: Structure of the pinning potential on the triangular (left) and square (right) lattices. Filled circles represent lattice sites at which the pinning potential is $-\epsilon$.

crystal with $\rho = \rho_I$ = 1/3, 2/3. On the square lattice, **Q** = $(4\pi/3, -2\pi/3)$ corresponds to a registered crystal at $\rho = \rho_C$ = 1/3, and **Q** = (π, π) to an incommensurate (checkerboard) crystal at $\rho = \rho_I$ = 1/2. Unless otherwise specified, these results discussed below pertain to a triangular lattice geometry. We have carried out careful extrapolation of the results to the thermodynamic limit. We have experienced that estimates obtained on a lattice of $L \times L = 576$ sites are identical, within statistical uncertainties, with the extrapolated ones.

We should note here that the pinning potentials have been chosen for definiteness to correspond to the commensurate density ρ_C = 1/4 for the triangular lattice, ρ_C = 1/3 for the square lattice (Fig. 4.11). No particular physical significance should be ascribed to these choices, as they are motivated only by the goal of making commensurate phases lower in density than the incommensurate ones, as would be the case for the second layer of ^{4}He on graphite, assuming a commensurate crystal exists. It seems reasonable to expect that the basic physical conclusions ought to remain unaffected by a different choice of pinning sublattice.

The purpose of this study is to provide a simple theoretical framework to interpret experimental studies probing for possible (commensurate) supersolid phases of helium films on graphite. Although we mostly discuss here numerical results obtained for a triangular lattice geometry, we have observed the same general physical behaviour on the square lattice as well.

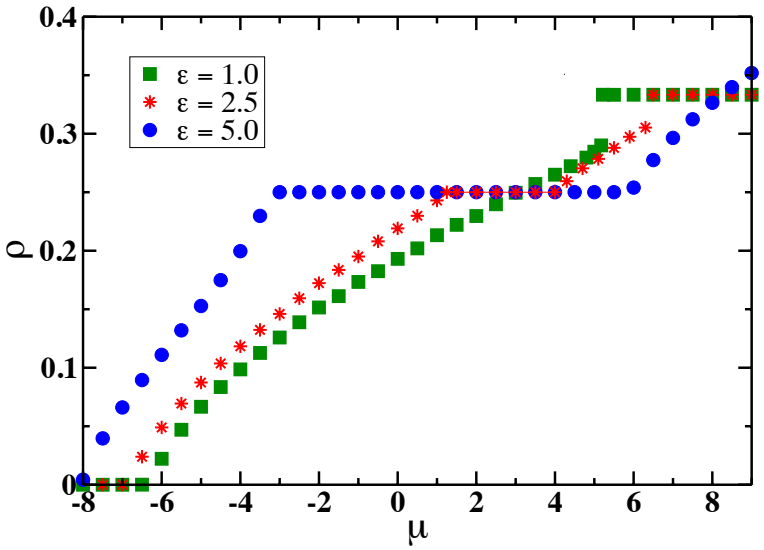

Figure 4.12: Density ρ versus chemical potential μ for V_1 = 6 and three different pinning potential strengths, namely ϵ = 1 (filled squares), ϵ = 2.5 (stars) and ϵ = 5 (filled circles). Statistical errors are smaller than symbol sizes. Results shown are for a triangular lattice with L = 24, and ρ_C = 1/4 is the commensurate (registered) crystal density, while ρ_I = 1/3 is the incommensurate crystal density.

4.2.2 The results

Our main finding is that supersolid phases exist on both the interstitial and on the vacancy side of a commensurate (registered) crystal. However, the superfluid density *always vanishes* as the density achieves a value corresponding to either a commensurate or incommensurate crystal. In this sense, the pinning potential does not give rise to fundamentally new behaviour, with respect to what is observed in this model near and/or at incommensurate crystal phases, in the absence of any external potential [18, 19, 20, 21, 22, 23, 24, 25, 26]. The vanishing of the superfluid response at crystal density, appears therefore to be a general hallmark of any phase labelled as "supersolid," occurring in a system of this type, i.e., in the presence of an external pinning potential.

We begin by discussing the existence of registered (commensurate) solid phases for sufficiently large values of ϵ, i.e., the strength of the adsorption potential.

Fig. 4.12 displays the density computed as a function of the chemical potential for V_1 = 6, for three different pinning potential strengths, namely ϵ = 1 (filled squares), ϵ = 2.5

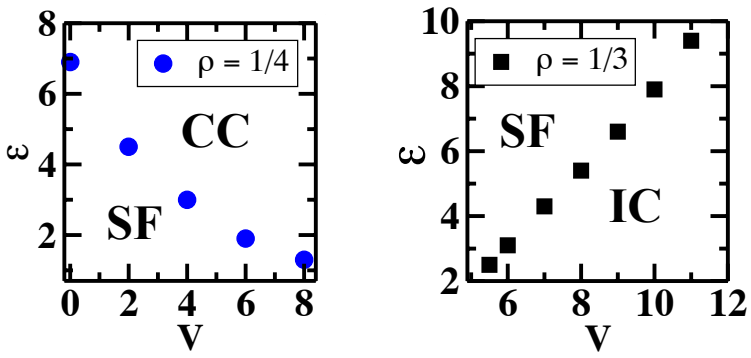

Figure 4.13: Ground state phase diagram of (4.2). Symbols lie at computed phase boundaries between a superfluid (SF) and a commensurate crystal (CC) for ρ = 1/4 (left), and between a superfluid and an incommensurate crystal (IC) at ρ = 1/3 (right). Statistical errors are smaller than symbol sizes.

(stars) and ϵ = 5 (filled circles). The value of V_1 is large enough for the incommensurate solid phases to exist, in the model without pinning potential.

For a weak pinning potential, plateaus in the density appear only at $\rho = \rho_I$ = 1/3 and ρ = 2/3, i.e., in correspondence of the incommensurate phases. A discontinuity of the curve signals a first-order phase transition between a superfluid and the incommensurate crystal. Analogously to what is observed in the model without pinning potential [22, 23, 24, 25, 26], for sufficiently large V_1 the $\rho(\mu)$ curve is continuous on the interstitial side ($\rho > \rho_I$), as a supersolid phase exists.

As the strength of the pinning potential is increased, two additional crystalline phases appear, one at $\rho = \rho_C$ = 1/4, the other at ρ = 5/8. Henceforth, we shall focus our attention on the phase of density ρ_C, which is registered with the pinning potential. The other phase arises from the competition between the pinning potential and the nearest-neighbour repulsion, and the basic physics at or near this density is the same as near ρ_C. As shown in Fig. 4.12, the $\rho(\mu)$ curve displays no discontinuities on either the vacancy or the interstitial side of the commensurate crystal. This is evidence of vacancy- and interstitial-doped supersolids, as we discuss below.

On performing a sufficient number of runs in the (V_1, ϵ) plane, we have computed the phase boundary lines shown in Fig. 4.13, between a superfluid and crystal at the two densities ρ_C and ρ_I. The left part of the figure refers to ρ_C. The system is superfluid for

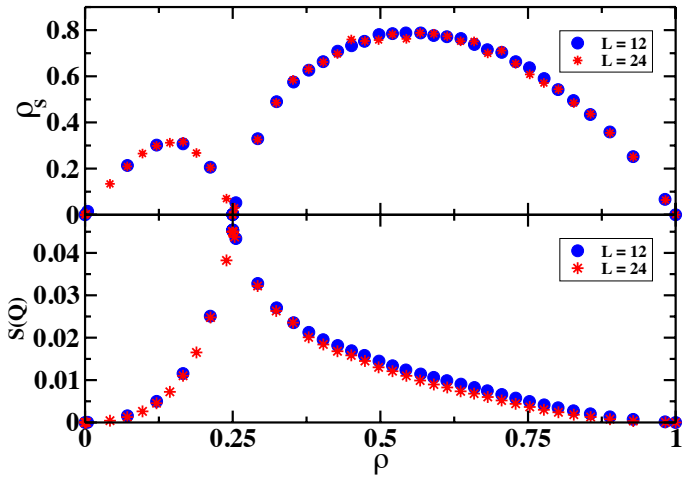

Figure 4.14: Superfluid density ρ_S (upper panel) and static structure factor S($\mathbf{Q}$) (lower panel) in case of V_1 = 4.0, ϵ = 5.0 and a wave vector $\mathbf{Q} = (\pi, 2\pi/\sqrt{3})$. Statistical errors are smaller than symbol sizes.

$\epsilon < \epsilon_c(V_1)$, where $\epsilon_c(V_1)$ is the minimum strength of the pinning potential for which a commensurate crystal is present, as a function of the strength of the nearest-neighbour repulsion V_1. For the commensurate phase $\epsilon_c(V_1)$ is monotonically decreasing with V_1, as the presence of a strong nearest-neighbour repulsion, which causes the appearance of the incommensurate crystalline phase at ρ_I = 1/3 also favours the formation of a commensurate crystal at ρ_C (in fact, $\epsilon_c(V_1)$ approaches zero as $V_1 \rightarrow \infty$). On the other hand, the right part of Fig. 4.13 shows that the pinning potential *suppresses* crystallization at density ρ_I, i.e., a *greater value* of V_1 is needed to stabilize the incommensurate crystal at ρ_I = 1/3 if the external pinning potential is present. This is due to the lattice mismatch of two competing crystalline phases. A sufficiently large value of ϵ causes the incommensurate phase to disappear altogether.

We now discuss the superfluid properties of the system near crystallization. We begin by examining the physics of the system near a commensurate solid phase. Fig. 4.14 shows the superfluid fraction ρ_S (upper panel) and the static structure factor S($\mathbf{Q} = (\pi, 2\pi/\sqrt{3})$) as a function of the particle density. The choice of parameters, namely V_1 = 4 and ϵ = 5, corresponds to a situation in which the only crystalline phase that the system forms is the

commensurate one, at a density ρ_C.

Both ρ_S and $S(\mathbf{Q})$ are everywhere *finite*, except at exactly ρ_C where the superfluid response vanishes. The fact that $\rho(\mu)$ is continuous everywhere, allows one to rule out coexistence of two phases (superfluid and crystal) possessing only one of the two types of order. Thus, based on its strict definition, one would have to conclude that this system is everywhere "supersolid," except at commensurate density. However, such a denomination appears to be meaningful (if at all) only in the vicinity of ρ_C, where the physical character of the phase can be surmised to be that of a commensurate crystal doped with either vacancies or interstitials. Away from ρ_C, the nature of the system is basically that of a fluid with a density modulation arising from the pinning potential. There is clearly an important conceptual difference between a physical system in which the breaking of translational invariance occurs spontaneously, and one in which it is induced by an external potential. Indeed, the very use of the terminology "supersolid" in the latter case may be questionable.

That at *exactly* $\rho = \rho_C$ the superfluid fraction vanishes, is a significant result that warrants a few comments. Supersolidity in model (4.2) on the triangular lattice (it is not present on the square lattice), requires that a crystal be doped with interstitial particles, i.e., the superfluid density of an undoped crystal is always zero [22, 23, 24, 25, 26]. However, one might speculate that the lower density commensurate phase stabilized by the external potential might enjoy different properties than the incommensurate one, which is the only one observed in the absence of a pinning potential. We find, however, that the superfluid density always vanishes at ρ_C, on both lattice geometries considered here. We have also repeated the same analysis for different choices of the parameters, including those for which both commensurate and incommensurate phases exists, but the presence of an incommensurate phase at higher density does not alter the physics of the system in the vicinity of ρ_C, i.e., a "supersolid" phase exists on both the interstitial and vacancy sides, but not at commensuration.

This is a result of potential experimental relevance, as studies of adsorbed ^{4}He films on corrugated substrate on graphite, for which claims of possible supersolid behaviour near commensurate density are made, can determine the superfluid response as a function

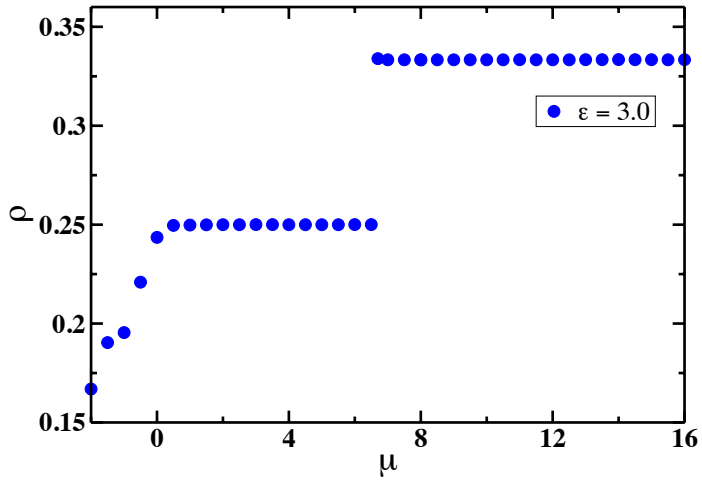

Figure 4.15: Density ρ versus chemical potential μ for the ground state of (4.2), with V_1 = 8, ϵ = 3. The density jump signals a first-order phase transition between a commensurate and an incommensurate crystal.

of coverage. It appears from our results that, to the extent that (4.2) can be regarded as a reasonable qualitative model of a thin helium film on a corrugated substrate, the superfluid signal must vanish at the coverage corresponding the occurrence of a commensurate crystal, if one is to make a claim of a "supersolid" phase near or at commensuration.

The physics of the system near the incommensurate crystal phase is the same as in the absence of an external potential [22, 23, 24, 25, 26]. In particular, the superfluid density again always vanishes at ρ_I. Here too, one might have expected that the weakening of the incommensurate crystal caused by the pinning potential could give rise to a "softer" crystalline phase, capable of superflow. What is observed, however, is that as long as the incommensurate crystal exists, the superfluid density at ρ_I vanishes. There is always a first-order phase transition on the vacancy side; on the other hand, on the interstitial side, depending on the value of V_1 one may have a first-order phase transition to a superfluid or a second-order phase transition to a supersolid.

We now consider the regime in which both the commensurate and incommensurate phases exist, and explore the quantum phase transitions between the two, with the possible occurrence of intervening phases. There are two possible scenarios which have been

observed: one is a direct transition from the commensurate to the incommensurate crystal, through a first order transition. In other words, there is only a jump in the curve $\rho(\mu)$ from ρ_C to ρ_I, as shown in Fig. 4.15. This occurs roughly in a regime where $\epsilon << V_1$, and is a scenario that appears to apply to the first layer of helium on graphite [69], or to films of molecular hydrogen adsorbed on graphite, or other corrugated substrates [74, 75].

The other scenario, occurring for $\epsilon \sim V_1$, is a second-order transition from the commensurate crystal at ρ_C to a doped supersolid phase, and then, as the density is increased, to a superfluid, followed by a first order phase transition from the superfluid to the incommensurate crystal at ρ_I. The transition from supersolid to superfluid is indicated by the change in slope of the $\rho(\mu)$ curve. We should note that this superfluid phase with modulated density arises from the pinning potential.

4.3 Disorder-induced superfluidity

4.3.1 The *attractive* interaction V_1 model

We describe a disordered Bose system by the following Hamiltonian (similarly to (4.2)):

$$H = -J \sum_{\langle ij \rangle} (\hat{a}_i^\dagger \hat{a}_j + h.c.) + V_1 \sum_{\langle ij \rangle} \hat{n}_i \hat{n}_j + \sum_i \delta_i \hat{n}_i \tag{4.3}$$

We only consider here a square lattice of $N = L \times L$ sites, with periodic boundary conditions. We model disorder by means of a random on-site potential δ_i, uniformly distributed in the interval $[-\Delta, \Delta]$. Other theoretical representations of a disordered environment could be considered, e.g., one in which the hopping matrix element J is randomly varied from site to site, but in this work we restrict ourselves to the above, widely adopted *diagonal* model of disorder [76, 77, 78, 79, 80]. In the spin language, the disordering potential is equivalent to a random on-site magnetic field along the z axis.

For the nearest-neighbour interaction, essentially all previous work based on (4.3) has focused on the *repulsive* case, i.e. $V_1 > 0$, chiefly to elucidate the nature of the disorder-driven superfluid to insulator transition [76, 77, 78, 80]. However, an *enhancement* of superfluidity by disorder has been predicted in some cases [79]. In this context, we here consider the case of an *attractive* nearest-neighbour interaction (i.e., $V_1 = -|V|$), and also

neglect interactions among particles beyond nearest neighbours, e.g. the next nearest V_2. With this choice, the Hamiltonian (4.3), which is essentially a lattice model of quantum "sticky" spheres, is isomorphic to that of a spin-1/2 XXZ quantum ferromagnet.

Disordered Bose systems have been the subject of intense study for two decades [11]. Most of the theoretical investigative effort has been focused on the quantum phase transition between a superfluid and insulating phase within the context of the Bose Hubbard model. For example, it has been established that disorder leads to the appearance of an (insulating) Bose glass, sandwiched between the superfluid and Mott insulating phases [11]. This topic is enjoying continued interest, especially since cold atom physicists have recently produced controllable disorder using laser speckles [81, 82, 83] and looked at such phenomena as Anderson localization in a one-dimensional condensate [84] and the suppression of the condensate fraction in three dimensions [83].

In the absence of disorder, the ground state of (4.3) is a superfluid for $|V_1| < 2$, whereas for $|V_1| \geq 2$ only a Mott insulating phase exists, with exactly one particle per site, regardless of lattice geometry and dimensionality. This is simply because the system can maximally lower its energy by having each particle surrounded by as many nearest-neighbouring particles as possible, trumping any contribution from the hopping term. The regime of interest in this work is the latter, i.e., that in which no superfluid phase exists in the absence of disorder.

The idea of a "superglass" has come to the forefront in the context of the investigation of the (super)solid ^{4}He. The superglass phase was initially observed in quantum Monte Carlo simulations, in which the superfluid phase had an inhomogeneous condensate map on a microscopic scale [85]. Biroli *et al.* proved that such a superglass phase does exist (at least as a metastable phase) by introducing an (artificial) model which could be mapped to a classical system of hard spheres and studied in a controlled fashion [86]. Recent experiments on solid ^{4}He have confirmed the strong interplay between a superfluid component and a slow (glassy) dissipative component. However, little is known yet about the superglass phase, nor specifically about the actual role of disorder in promoting or enhancing superfluidity. Given the current controversies and puzzles surrounding the interpretation of experiments on the possible supersolid phase of helium, further investigations of superfluid glassy phases are warranted.

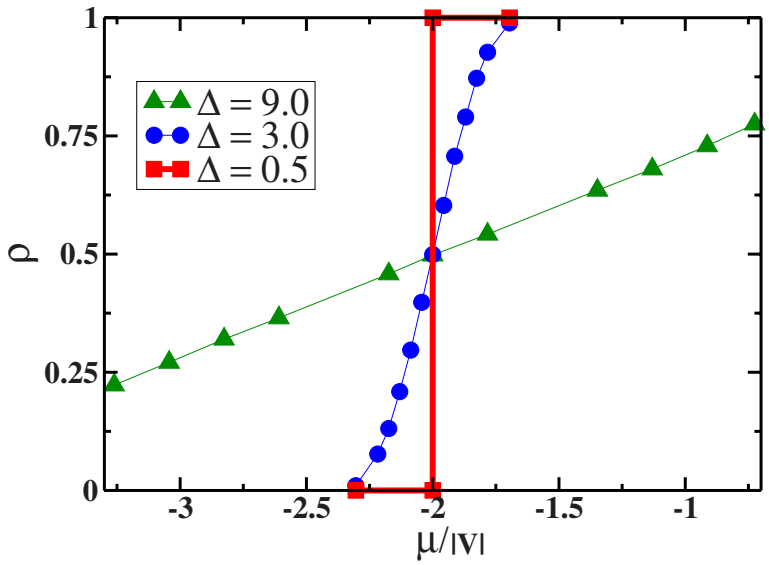

Figure 4.16: Ground state density ρ versus chemical potential μ for $|V_1| = 2.3$, for weak (Δ = 0.5, squares), intermediate (Δ = 3.0, circles) and strong (Δ = 9.0, triangles) disorder. Results shown are for a lattice of size L = 96, and are obtained by averaging over 20 independent realizations of the disorder. Statistical errors are smaller than symbol sizes.

4.3.2 The results

In this work, we provide strong numerical evidence for disorder-induced superfluidity in a lattice realization of hard-core bosons with a strong nearest-neighbor attraction, in the presence of external disorder. In particular, we show here that at low temperature and in a small range of attractive interactions, disorder of sufficient strength stabilizes a "glassy" superfluid phase. The superfluid density reaches a maximum and then decays as the strength of the disorder increases, as an insulating glassy phase intervenes.

In contrast to the case of repulsive bosons where disorder reduces the size of the superfluid phase, we see that strongly attracting hard-core bosons can be stabilized and made superfluid by disorder. In other words, disorder *induces* superflow in an otherwise insulating phase. Aside from supersolid ^{4}He, such a scenario is possibly relevant to other condensed matter systems, e.g., high-temperature superconductors [27], as well as to the elusive superfluid phase of molecular hydrogen [28], and to the role of substrate disorder in the superfluidity of (sub)monolayer helium films [30].

Fig. 4.16 shows the average particle density ρ as a function of the chemical potential

μ, for a particular value of $|V_1|$ greater than 2 ($|V_1|$ = 2.3). For weak disorder (i.e., small Δ), the ground state of the system has exactly one particle per site, with an abrupt density jump at $\mu/|V_1| = 2$, when the lattice turns from empty to fully filled. However, for disorder of sufficient strength (figure shows results for Δ = 3), the density jump disappears, being replaced by a smooth curve, signaling continuous dependence of density on chemical potential. In other words, the disorder stabilizes phases at intermediate densities, consisting of interconnected "clusters" of particles, pinned by local fluctuations of the disordering potential. In this situation, the value $\mu/|V_1| = 2$ corresponds to a particle density $\rho = 0.5$.

Clearly, the issue immediately arises of whether such disordered phases may turn superfluid at low T, and what the nature would be of such a disordered superfluid phase, simultaneously featuring broken translational invariance.

We investigated the occurrence of superfluid behaviour by directly calculating the superfluid density ρ_S (using the standard winding number estimator). Fig. 4.17 shows ρ_S as a function of particle density ρ, in the limit $T \to 0$, for one of the choices of model parameters of Fig. 4.16, namely Δ = 3 and $|V_1|$ = 2.3. The superfluid density increases from zero and reaches a maximum value at half filling, where approximately 12% of the system is superfluid.

Obviously, numerical data such as those shown in Fig. 4.17 must be extrapolated to the $L \to \infty$, in order for us to be able to make confidently the statement that superfluidity observed in these systems is not merely a finite-size effect but survives in the thermodynamic limit. The inset of Fig. 4.17 shows a typical extrapolation; estimates are shown for the superfluid density obtained for a fixed particle density $\rho = 0.5$, on square lattices of different sizes (12, 24, 48 and 96), for $|V_1|$ = 2.3 and Δ = 3. It is worth restating that these estimates are obtained by averaging results corresponding to several independent realizations of the disordering potential. Based on results such as those shown in the inset of Fig. 4.17, we conclude that the superfluid signal remains finite in the thermodynamic limit. In general, we have observed that results obtained on a lattice with L = 96 offer a close representation of the physics of the thermodynamic limit, at least in the range of parameters discussed here.

The observed superfluid phase is ostensibly induced by disorder, which stabilizes uniform phases of filling intermediate between zero and one. In order to gain further insight

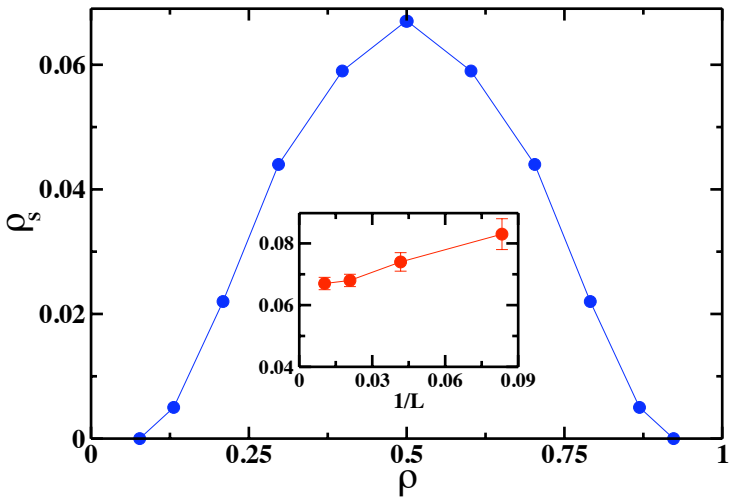

Figure 4.17: Superfluid density ρ_S versus particle density ρ for $|V_1|$ = 2.3 and disorder strength Δ = 3. Statistical errors are smaller than symbol sizes. Results shown are for a square lattice with L = 96, and β = L, and are obtained by averaging over 20 independent realizations of the disorder. The solid line is a guide to the eye. *Inset*: Superfluid density for a fixed particle density ρ = 0.5, computed on square lattices of varying size L. Extrapolation to infinite system size still gives a finite superfluid density.

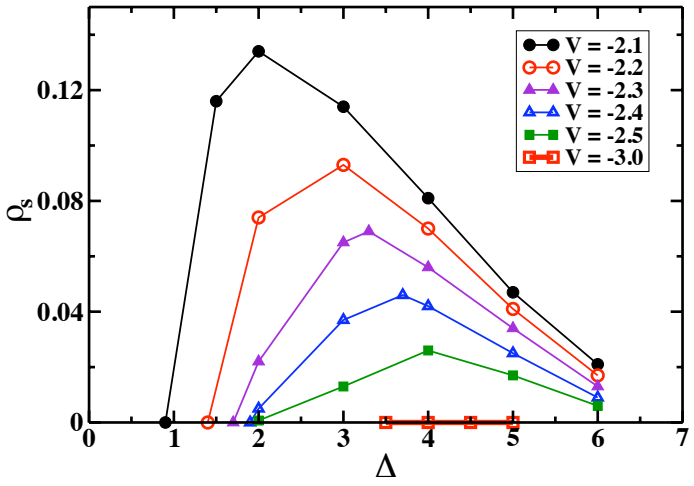

Figure 4.18: Maximum value of the superfluid density ρ_S (attained for ρ = 0.5) versus disorder strength Δ for different attractive interactions V_1. Statistical errors are smaller than symbol sizes. Solid lines are only meant to guide the eye.

and in-depth understanding of the role of disorder in actually promoting superfluidity, it is of interest to study the competition between the strength of disorder (Δ) and that of the attractive boson interaction ($|V_1|$). For definiteness, we consider the case of half filling, corresponding to a maximum in the superfluid density (for those systems for which superfluidity is observed). The same trends are also observed away from half filling.

When the disorder is weak ($\Delta \ll |V_1|$), it cannot break apart clusters of particles, hence the system remains insulating, as shown in Fig. 4.18 or by the vanishing compressibility $\kappa = d\rho/d\mu$ for Δ = 0.5 in Fig. 4.16. There are thus macroscopic domains (empty or fully filled) with hidden long-range order in the system [87, 88]. When the disorder becomes of the order of the attraction ($\Delta \leq |V_1|$), sites and regions begin to appear throughout the system where the chemical potential is low enough to rip particles off the cluster, which then breaks down into large grains. These particles, however, are still largely localized in the vicinity of the energetically favourable sites created by disorder, and therefore transport remains weak, as the curve for Δ = 2 in Fig. 4.19 shows.

If we further increase the disorder strength, the grain size decreases to a microscopic scale, a (relatively) large fraction of the particles are delocalized, and superfluidity along

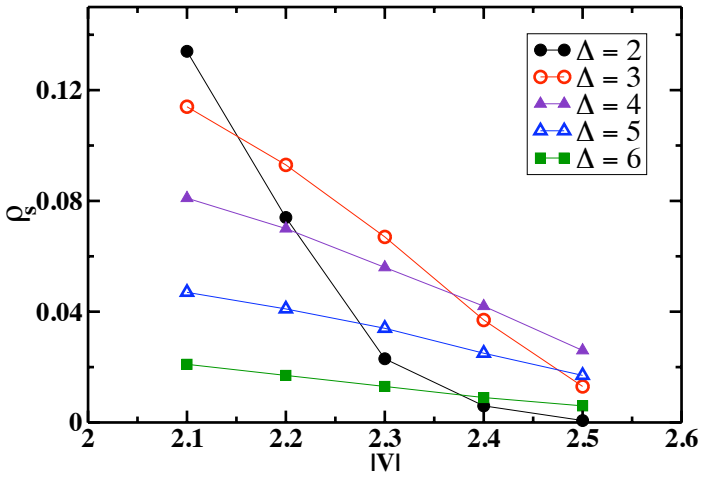

Figure 4.19: Maximum value of the superfluid density ρ_S (attained for ρ = 0.5) versus absolute value of attractive interaction $|V_1|$ for different diagonal disorder Δ at inverse temperature β = 96. Statistical errors are smaller than symbol sizes. Results shown are for a square lattice with L = 96. The solid lines are a guide to the eye.

interfaces (ridges) becomes possible, as also shown in previous numerical studies [85, 89]. This effect takes place essentially due to percolation. We can thus say that the disorder counters the insulating trend caused by the attractions, and actually makes the system superfluid. This is shown in Fig. 4.18 where we see a rather large superfluid fraction as a function of disorder. Naturally, as the disorder strength is increased even further, insulating glassy behaviour re-appears, because the disorder is now so strong that it can block any superfluid path and localize particles, much as in the case of repulsive interactions.

A similar scenario takes place on increasing the interaction strength $|V_1|$ at constant disorder bound Δ, as shown in Fig. 4.19. We have already explained the steep decay of the curve corresponding to $\Delta = 2 < |V_1|$ above, due to the lack of carriers. When Δ is greater than $|V_1|$, the disorder is sufficiently strong to destroy all macroscopic domains, and superfluidity can occur all over the sample. But as the disorder becomes stronger, it prevents particle world lines from winding around the lattice. In the regime of strong disorder, both the disorder and the attractive interactions contribute to suppress superfluidity,

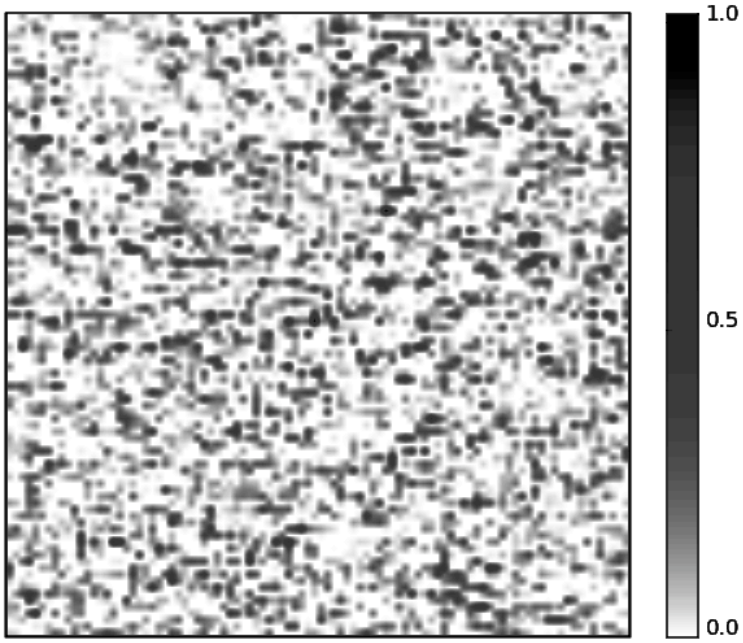

Figure 4.20: Map of the local superfluid density for a particular disorder realization, on a square lattice with L = 96, $|V_1|$ = 2.3 and Δ = 3. The total superfluid density ρ_S equals 0.068(1) for this run. The white areas are small insulating grains, connected by superfluid interfaces.

as regions with nearly uniform chemical potential will be insulating due to the strong attraction, which pulls particles together in such regions.

It is worth noting that the above scenario is quite different from that of the repulsive disordered Bose-Hubbard model, where regions of uniform chemical potential are crucial for stabilizing locally a liquid phase, and thus the superfluid properties and the compressibility of the whole system [11]. We also note here that this insulating phase is compressible, as shown in Fig. 4.16 for Δ = 9, which justifies the nomenclature "Bose glass" [11]. The compressibility at half filling goes from zero in the phase segregated regime (no disorder), to a large value in the superfluid phase, and decreases then monotonically over the Bose glass phase, when increasing the disorder bound at constant interaction strength.

This "superglass" phase can be visualized through local superfluid density maps, shown in Fig. 4.20, for a particular realization of disorder. The local value is obtained by statistically averaging local contributions to the total superfluid density (i.e., to the square of the winding number), which, in the case shown in Fig. 4.20 for Δ = 3 and $|V_1|$ = 2.3,

amounts to slightly less than 7%. We found that the covariance between the superfluid density and the disordering potential is virtually zero, i.e., for these values of the parameters the physics is mostly driven by the attraction between bosons, consistent with the picture given above in the case of strong disorder and strong attraction.

Chapter 5

Summary and conclusions

We have investigated superfluidity in a system of lattice hardcore bosons, with the inclusion of interactions between particles residing on nearest-neighbouring and next-nearest-neighbouring sites. The purpose of this study is to gain understanding of the occurrence of superfluidity in concomitance with, or near, particle localization. In our studies, localization arises either from spontaneous crystallization occurring as a result of the interactions among elementary constituents, or it is induced by an external "pinning" potential, periodic or random. Using state-of-the-art QMC methodology, we have studied the phase diagrams at low temperature (ground state) of the system in the physical settings described above.

First, we have investigated the scenario in which a supersolid phase occurs near crystallization induced by inter-particle interactions. This study was carried out in the context of the $V_1 - V_2$ model on the square lattice, where the system forms a crystalline phase at a quarter filling for sufficiently strong next-nearest-neighbour interaction. Our results show that a vacancy-based supersolid phase is stable, in striking contrast with what is observed on the triangular lattice. We have obtained a simple criterion to predict the occurrence of vacancy- and interstitial-based supersolid phases, which accounts for all of the theoretical results obtained so far. These predictions should be observable with existing experimental techniques, for example with polar molecules in optical lattices [63].

Second, we have studied possible supersolid behaviour close to a crystalline phase stabilized by an external periodic "pinning potential," which plays the same role as the

adsorption sites of a corrugated substrate. In the absence of an external potential, such a crystalline phase is not present in the phase diagram of the system. Our main finding is that in specific circumstances "supersolid" phases can exist in the vicinity (on both the interstitial and the vacancy sides) of commensurate crystals stabilized by the adsorption potential. A distinctive signature of the occurrence of such phases is the vanishing of the superfluid density at commensuration. This seems to be a universal feature of this type of system, one that we would expect to see in any experiment claiming observation of a supersolid phase of adsorbed films (e.g., of ^{4}He) on substrates such as graphite. Our main findings are independent of the lattice geometry and/or potential periodicity. It is also worth mentioning that these predictions may also lend themselves to possible experimental verification by means of ultracold atoms in optical lattices [14].

Finally, we have investigated a different scenario of superfluidity, arising from the presence of disorder. Our results yield strong evidence for disorder-induced superfluidity with a strong *attractive* nearest-neighbour interaction. While the system without disorder is an insulator of the ferromagnetic Ising type, disorder can induce an inhomogeneous superfluid (or "superglass" [85]) phase (corresponding to in-plane order in the spin nomenclature) over a range of interaction and disorder strengths. For stronger disorder bounds, the disorder and the attractive interactions work together to localize the particles. In the absence of disorder, the physics of our model is reminiscent to that of molecular *para*-hydrogen, long speculated to be a potential "second superfluid," due to the light mass of its constituents (one half that of helium atoms). On the other hand, superfluidity is not observed in *para*-hydrogen due to the strength of the intermolecular potential, which causes the system to crystallize at temperatures significantly above that at which Bose Condensation is expected to take place [90]. Recent numerical studies [28] have shown that disorder ought *not* give rise to a superfluid phase of *para*-hydrogen. Based on the results obtained in this work, we may argue that *para*-hydrogen may be a system too "deep" in the insulating regime (i.e., the effective value of nearest neighbour interaction $|V_1|$ is too large) for disorder to stabilize a superfluid phase. On the other hand, the results obtained here suggest that disorder may be responsible for the observation of superfluidity in helium films at coverages corresponding to less than a full monolayer. It should be noted, though, that helium films are expected to be superfluid at "negative" pressure, in

fact all the way down to the spinodal density [91], so that they are quite different from the system considered here. Such coherence induced by disorder might easily be observable in time-of-flight images for ultracold atoms or molecules [92].

One can see that the interplay between superfluidity and localization in a system of strongly correlated Bose particles results in very rich physics, and, as outlined above, our study of this paradigm, using extensive state-of-the-art computer simulations, has revealed several features with direct implications for the contentious topic of supersolidity and superglass.

Significant effort is currently being exerted to better understand the supersolid and superglass phases of matter. Of the various open questions remaining, it is still necessary to address the nature of supersolidity as well as the physics of the superglass phase in Helium-4, which remain controversial in part due to a lack of knowledge regarding the influence of impurities. As an extension of the work presented in this thesis, it would be interesting to study the mechanisms behind these phases.

Bibliography

[1] P. Kapitza. *Nature*, 141:74, 1938.

[2] J. F. Allen and A. D. Misener. *Nature*, 141:75, 1938.

[3] F. London. *Phys. Rev.*, 54:947, 1938.

[4] L. Tisza. *Nature*, 141:913, 1938.

[5] A. Griffin, D. W. Snoke, and S. Stringari. *Bose-Einstein condensation*. Cambridge, 1995.

[6] D. R. Tilley and J. Tilley. *Superfluidity and Superconductivity (Graduate Student Series in Physics)*. Taylor and Francis, 1990.

[7] A. F. Andreev and I. M. Lifshitz. *Sov. Phys. JETP*, 29:1107, 1969.

[8] G. V. Chester. *Phys. Rev. A*, 2:256, 1970.

[9] A. J. Leggett. *Phys. Rev. Lett.*, 25:1543, 1970.

[10] E. Kim and M. Chan. *Nature*, 427:225, 2004.

[11] M. P. Fisher, P. B. Weichman, G. Grinstein, and D. S. Fisher. *Phys. Rev. B*, 40:546, 1989.

[12] D. Jaksch, C. Bruder, J. I. Cirac, C. W. Gardiner, and P. Zoller. *Phys. Rev. Lett.*, 81:3108, 1998.

[13] D. Jaksch and P. Zoller. *Ann. Phys.*, 315:52, 2005.

[14] I. Bloch, J. Dalibard, and W. Zwerger. *Rev. Mod. Phys.*, 80:885, 2008.

[15] N. V. Prokof'ev, B. V. Svistunov, and I. S. Tupitsyn. *JETP*, 87:310, 1998.

[16] N. V. Prokof'ev, B. V. Svistunov, and I. S. Tupitsyn. *Phys. Lett. A*, 238:253, 1998.

[17] M. Boninsegni, A. B. Kuklov, L. Pollet, N. V. Prokof'ev, B. V. Svistunov, and M. Troyer. *Phys. Rev. Lett.*, 97:080401, 2006.

[18] G. G. Batrouni and R. T. Scalettar. *Phys. Rev. Lett.*, 84:1599, 2000.

[19] F. H*é*bert, G. G. Batrouni, R. T. Scalettar, G. Schmid, M. Troyer, and A. Dorneich. *Phys. Rev. B*, 65:014513, 2001.

[20] Y. C. Chen, R. G. Melko, S. Wessel, and Y. J. Kao. *Phys. Rev. B*, 77:014524, 2008.

[21] P. Sengupta, L. P. Pryadko, F. Alet, M. Troyer, and G. Schmid. *Phys. Rev. Lett.*, 94:207202, 2005.

[22] M. Boninsegni. *J. Low. Temp. Phys.*, 32:139, 2003.

[23] R. G. Melko, A. Paramekanti, A. A. Burkov, A. Vishwanath, D. N. Sheng, and L. Balents. *Phys. Rev. Lett.*, 95:127207, 2005.

[24] M. Boninsegni and N. Prokof'ev. *Phys. Rev. Lett.*, 95:237204, 2005.

[25] M. Troyer S. Wessel. *Phys. Rev. Lett.*, 95:127205, 2005.

[26] D. Heidarian and K. Damle. *Phys. Rev. Lett.*, 95:127206, 2005.

[27] J. C. Phillips. *PNAS*, 105:9917, 2008.

[28] J. Turnbull and M. Boninsegni. *Phys. Rev. B*, 78:144509, 2008.

[29] H. Cho and G. A. Williams. *Phys. Rev. Lett.*, 75:1562, 1995.

[30] G. A. Csáthy, J. D. Reppy, and M. H. W. Chan. *Phys. Rev. Lett.*, 91:235301, 2003.

[31] G. T. Zimanyi, P. A. Crowell, R. T. Scalettar, and G. G. Batrouni. *Phys. Rev. B*, 50:6515, 1994.

[32] M. Cha, M. P. A. Fisher, S. M. Girvin, M. Wallin, and A. P. Young. *Phys. Rev. B*, 44:6883, 1991.

[33] E. S. Sorensen, M. Wallin, S. M. Girvin, and A. P. Young. *Phys. Rev. Lett.*, 69:828, 1992.

[34] R. R. Scalettar, G. G. Batrouni, and G. T. Zimanyi. *Phys. Rev. Lett.*, 66:3144, 1991.

[35] K. G. Singh and D. S. Rokhsar. *Phys. Rev. B*, 46:3002, 1992.

[36] M. Kohno and M. Takahashi. *Phys. Rev. B*, 56:3212, 1997.

[37] M. Greiner, O. Mandel, T. Esslinger, T. Hänsch, and I. Bloch. *Nature*, 415:39, 2002.

[38] H. Sheshadri, H. R. Krishnamurty, R. Pandit, and T. V. Ramakrishnan. *Europhys. Lett.*, 22:257, 1993.

[39] R. T. Scalettar, G. G. Batrouni, A. P. Kampf, and G. T. Zimanyi. *Phys. Rev. B*, 51:8467, 1994.

[40] L. Amico and V. Penna. *Phys. Rev. Lett.*, 80:2189, 1998.

[41] L. Dang, M. Boninsegni, and L. Pollet. *Phys. Rev. B*, 78:132512, 2008.

[42] R. G. Melko, A. Del Maestro, and A. A. Burkov. *Phys. Rev. B*, 74:214517, 2006.

[43] H. F. Trotter. *Proc. Am. Math. Soc.*, 10:545, 1959.

[44] M. Suzuki. *Prog. of Theor. Phys.*, 76:1454, 1976.

[45] R. J. Baxter. *Exactly Solved Models in Statistical Mechanics*. Academic Press, London, 1982.

[46] H. Gould, J. Tobochnik, and W. Christian. *An Introduction to Computer Simulation Methods: Applications to Physical Systems*. Addison Wesley, 3rd Edition, 2006.

[47] N.Metropolis, A.W.Rosenbluth, M.N.Metropolis, A.H.Teller, and E.Teller. *J. Chem. Phys.*, 21:1087, 1953.

[48] B. A. Berg. *Markov Chain Monte Carlo Simulations and Their Statistical Analysis*. Singapore, World Scientific, 2004.

[49] R. H. Swendsen and J. S. Wang. *Phys. Rev. Lett.*, 58:86, 1987.

[50] U. Wolff. *Phys. Rev. Lett.*, 60:1461, 1988.

[51] A. W. Sandvik. *Phys. Rev. B*, 59:14157, 1999.

[52] O. F. Syljuåsen and A. W. Sandvik. *Phys. Rev. E*, 66:046701, 2002.

[53] N. Prokof'ev. *Theory of Monte Carlo Methods*, Lecture Notes.

[54] L. Pollet, K. V. Houcke, and S. M. A. Rombouts. *J. Comput. Phys.*, 225:2249, 2007.

[55] A. Fetter and J. Walecka. *Quantum Theory of Many-Particle Systems*. Dover Publications, 2003.

[56] D.M. Ceperley. *Rev. Mod. Phys.*, 67:279, 1995.

[57] M. Troyer, F. Alet, S. Trebst, and S. Wessel. *AIP Conf. Proc.*, 690:156, 2003.

[58] O. Kallenberg. *Foundations of Modern Probability*. New York, Springer-Verlag, 1997.

[59] J. S. Liu. *Monte Carlo Strategies in Scientific Computing*. Springer Verlag, 1999.

[60] M. Troyer. *Lecture notes for ORNL workshop on Wang-Landau sampling*. 2003.

[61] S. V. Isakov, S. Wessel, R. G. Melko, K. Sengupta, and Y. B. Kim. *Phys. Rev. Lett.*, 97:147202, 2006.

[62] S. Wessel. *Phys. Rev. B*, 75:174301, 2007.

[63] H. P. B*ü*chler, M. Lukin, A. Micheli, N. Prokof'ev, G. Pupillo, and P. Zoller. *Phys. Rev. Lett.*, 98:060404, 2007.

[64] L. W. Bruch, M. W. Cole, and E. Zaremba. *Physical Adsorption: Forces and Phenomena*. Clarendon Press, Oxford, 1997.

[65] D. S. Greywall and P. A. Busch. *Phys. Rev. Lett.*, 67:3535, 1991.

[66] P. A. Crowell and J. D. Reppy. *Phys. Rev. Lett.*, 70:3291, 1993.

[67] P. A. Crowell and J. D. Reppy. *Phys. Rev. B*, 53:2701, 1996.

[68] Shibayama, H. Fukuyama, and K. Shirahama. *J. Phys:Conference Series*, 150:032096, 2009.

[69] P. Corboz, M. Boninsegni, L. Pollet, and M. Troyer. *Phys. Rev. B*, 78:245414, 2008.

[70] L. Dang, M. Boninsegni, and L. Pollet. *Phys. Rev. B*, 79:214529, 2009.

[71] G. T. Zimanyi, P. A. Crowell, R. T. Scalettar, and G. G. Batrouni. *Phys. Rev. B*, 50:6515, 1994.

[72] C. E. Campbell, F. J. Milford, A. D. Novaco, and M. Schick. *Phys. Rev. A*, 6:1648, 1972.

[73] G. Zimmerli, G. Mistura, and M. H. W. Chan. *Phys. Rev. Lett.*, 68:60, 1992.

[74] J. Turnbull and M. Boninsegni. *J. Low Temp. Phys.*, 140:269, 2005.

[75] J. Turnbull and M. Boninsegni. *Phys. Rev. B*, 76:104524, 2007.

[76] M. Makivic, N. Trivedi, and S. Ullah. *Phys. Rev. Lett.*, 71:2307, 1993.

[77] M. Wallin, E. S. Sorensen, S. M. Girvin, and A. P. Young. *Phys. Rev. B*, 49:12115, 1994.

[78] F. Alet and E. S. Sorensen. *Phys. Rev. E*, 67:015701, 2003.

[79] W. Krauth, N. Trivedi, and D. Ceperley. *Phys. Rev. Lett.*, 67:2307, 1991.

[80] N. Prokof'ev and B. Svistunov. *Phys. Rev. Lett.*, 92:015703, 2004.

[81] J. Billy, V. Josse, Z. Zuo, A. Bernard, B. Hambrecht, P. Lugan, D. Clément, L. Sanchez-Palencia, P. Bouyer, and A. Aspect. *Nature*, 453:891, 2008.

[82] L. Sanchez-Palencia, D. Clément, P. Lugan, P. Bouyer, and A. Aspect. *New J. Phys.*, 10:045019, 2008.

[83] M. White, M. Pasienski, D. McKay, S. Zhou, D. Ceperley, and B. DeMarco. *Phys. Rev. Lett.*, 102:055301, 2009.

[84] G. Roati, C. D'Errico, L. Fallani, M. Fattori, C. Fort, M. Zaccanti, G. Modugno, M. Modugno, and M. Inguscio. *Nature*, 453:895, 2008.

[85] M. Boninsegni, N. V. Prokofev, and B. V. Svistunov. *Phys. Rev. Lett.*, 96:105301, 2006.

[86] G. Biroli, C. Chamon, and F. Zamponi. *Phys. Rev. B*, 78:224306, 2008.

[87] E. T. Seppälä, V. Petäjä, and M. J. Alava. *Phys. Rev. E*, 58:R5217, 1998.

[88] Y. Imry and S. K. Ma. *Phys. Rev. Lett.*, 35:1399, 1975.

[89] E. Burovski, E. Kozik, A. Kuklov, N. Prokof'ev, and B. Svistunov. *Phys. Rev. Lett.*, 94:165301, 2005.

[90] V. L. Ginzburg and A. A. Sobyanin. *JETP Lett.*, 15:242, 1972.

[91] M. Boninsegni, M. W. Cole, and F. Toigo. *Phys. Rev. Lett.*, 83:2002, 1999.

[92] L. Fallani, J. E. Lye, V. Guarrera, C. Fort, and M. Inguscio. *Phys. Rev. Lett.*, 98:130404, 2007.